AD-A264 704

WL-TR-93-3016

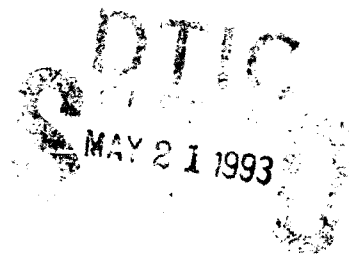# COMPUTATION OF A DELTA-WING ROLL-AND-HOLD MANEUVER

Raymond E. Gordnier
Miguel R. Visbal
Computational Fluid Dynamics Research Branch
Aeromechanics Division

February 1993

Final Report for Period 1 February 1992 - 1 February 1993

DTIC

MAY 21 1993

Approved for public release; distribution is unlimited.

FLIGHT DYNAMICS DIRECTORATE
WRIGHT LABORATORY
AIR FORCE SYSTEMS COMMAND
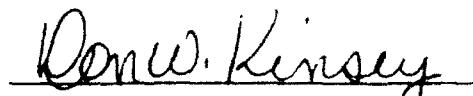WRIGHT-PATTERSON AIR FORCE BASE, OHIO 45433-7562
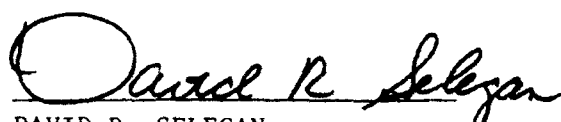
93-11323

93 5   032

NOTICE

When Government drawings, specifications, or other data are used for any purpose other than in connection with a definitely Government-related procurement, the United States Government incurs no responsibility or any obligation whatsoever. The fact that the government may have formulated or in any way supplied the said drawings, specifications, or other data, is not to be regarded by implication, or otherwise in any manner construed, as licensing the holder, or any other person or corporation; or as conveying any rights or permission to manufacture, use, or sell any patented invention that may in any way be related thereto.

This report is releasable to the National Technical Information Service (NTIS). At NTIS, it will be available to the general public, including foreign nations.

This technical report has been reviewed and is approved for publication.

RAYMOND E. GORDNIER
Aeospace Engineer
CFD Research Section

DON W. KINSEY
Actg Chief
CFD Branch

DAVID R. SELEGAN
Chief
Aeromechanics Division

If your address has changed, if you wish to be removed from our mailing list, or if the addressee is no longer employed by your organization please notify WL/FIMC , WPAFB, OH 45433-7913 to help us maintain a current mailing list.

Copies of this report should not be returned unless return is required by security considerations, contractual obligations, or notice on a specific document.

REPORT DOCUMENTATION PAGE

1. AGENCY USE ONLY (Leave blank)	2. REPORT DATE	3. REPORT TYPE AND DATES COVERED
	12 Feb 93	Final Report, 1 Feb 92 – 1 Feb 93

4. TITLE AND SUBTITLE	5. FUNDING NUMBERS
Computation of a Delta-Wing Roll-and-Hold Maneuver	PE: 61102F PR: 2307
6. AUTHOR(S) Raymond E. Gordnier Miguel Visbal	TA: N6 WU: 11

7. PERFORMING ORGANIZATION NAME(S) AND ADDRESS(ES)	8. PERFORMING ORGANIZATION REPORT NUMBER
Aerodynamic & Airframe Branch Aeromechanics Division Flight Dynamics Directorate Wright Laboratory (AFMC) Wright-Patterson AFB OH 45433-7562	WL-TR-93-3016

9. SPONSORING/MONITORING AGENCY NAME(S) AND ADDRESS(ES)	10. SPONSORING/MONITORING AGENCY REPORT NUMBER

11. SUPPLEMENTARY NOTES

12a. DISTRIBUTION/AVAILABILITY STATEMENT	12b. DISTRIBUTION CODE
Approved for public release; unlimited distribution	

13. ABSTRACT (Maximum 200 words)

This report presents computations of the flowfield around an 80 degree sweep delta wing undergoing a constant roll-rate maneuver from 0 to 45 degrees. The governing equations for the problem are the unsteady, three-dimensional Navier-Stokes equations. The equations are solved using the implicit, approximately-factored algorithm of Beam-Warming. Fixed roll angle results are also presented and compared with experimental measurements to demonstrate the ability of the numerical technique to accurately capture the flowfield around a rolled delta wing. The dynamic behaviors of the vortex position and strength, as well as their corresponding effect on surface pressure, lift and roll moment, are described. A simple, quasi-static explanation of these vortex behaviors based on effective angle-of-attack and sideslip angle is proposed.

14. SUBJECT TERMS		15. NUMBER OF PAGES
Delta Wing Roll, Vortex Dynamics, Vortical Flow, Unsteady Maneuver		46
		16. PRICE CODE

17. SECURITY CLASSIFICATION OF REPORT	18. SECURITY CLASSIFICATION OF THIS PAGE	19. SECURITY CLASSIFICATION OF ABSTRACT	20. LIMITATION OF ABSTRACT
Unclassified	Unclassified	Unclassified	Unlimited

Table of Contents

iii

List of Figures

List of Tables

Acknowledgements

List of Abbreviations and Symbols

CL $=$ lift coefficient

Cl $=$ roll moment coefficient

C_p $=$ pressure coefficient

E_t $=$ total energy

J $=$ transformation Jacobian

L $=$ root chord length

M_∞ $=$ freestream Mach number

p $=$ pressure

Pr $=$ Prandtl number

Re $=$ Reynolds number

S $=$ half-span

T $=$ temperature

t $=$ non-dimensional time $t = \frac{\tilde{t} u_\infty}{L}$

u, v, w $=$ velocity components in x, y and z

x, y, z $=$ physical coordinates

X, Y, Z $=$ body fixed coordinates

ξ, η, ζ $=$ computational coordinates

ρ $=$ density

μ_l $=$ laminar viscosity coefficient

μ_t $=$ eddy viscosity coefficient

$\vec{\omega}$ $=$ angular velocity

ϕ $=$ roll angle

$\dot{\phi}$ $=$ roll rate (rad/sec)

Φ $=$ non-dimensional roll rate, $\Phi = \frac{\dot{\phi} L}{u_\infty}$

τ_{ij} $=$ stress tensor

1. Introduction

The combat requirements for modern fighter aircraft necessitate that they be highly maneuverable and able to operate at high angle of attack. Since most fighter aircraft incorporate a delta-wing lifting surface, there has been great interest in studying the aerodynamics of delta wings. These flows are also rich in fundamental fluid mechanics phenomena, including longitudinal vortices, vortex breakdown, and shear-layer instability. Extensive experimental and computational studies of delta wing flows have been reported in the literature. An extensive review of computational techniques for modeling delta-wing flows has been given by Hoeijmakers [1].

More recently there has been an increasing interest in unsteady delta-wing maneuvers, including pitching to large incidence angle and high rate rolling motion. This unsteady flow environment introduces many interesting nonlinear aerodynamic phenomena. The inherent unsteadiness of the flowfields can also lead to aerodynamic behavior that may be advantageous or detrimental to aircraft performance. Understanding of this unsteady aerodynamic behavior will be vital in improving the design and performance of present and future fighter aircraft. Ericsson and Reding [2] have provided an extensive review of the fluid dynamics of these unsteady separated flows.

The predominant interest in roll maneuvers has been understanding the self-sustained wing rock phenomena observed for high sweep delta wings at moderate to large angles of attack. Several different experiments in both water and wind tunnels have investigated delta-wing rock through flow visualization and force and moment measurements [3-7]. Recently, Arena [8] has also reported unsteady surface pressure measurements for a rocking delta wing. These experiments have provided valuable insight into the mechanisms that lead to self-sustained wing rock. They are limited, however, by the difficulties encountered in taking measurements in a dynamic environment.

Numerical simulations of delta-wing rock provide an alternate means of investigating these rolling motions and compliment experimental measurements. Numerical simulations allow for the investigation of flow features that may be difficult or impossible to obtain experimentally. The majority of computations for rolling delta wings have assumed either conical [9-11] or inviscid [12]flow and their application is, therefore, limited. Chaderjian [13] has presented the first computations for wing rock using the three-dimensional, thin-layer Navier-Stokes equations.

The focus of the present work is the numerical simulation of a constant roll rate, $\Phi = 0.1325$, maneuver from $0°$ to $45°$. The study of this "roll-and-hold" maneuver is useful in understanding the aerodynamics of a maneuvering fighter aircraft. While this transient maneuver does not contain the full wing-rock

motion, many of the aerodynamic features observed are also common to wing rock. These computations therefore, provide valuable information and insight before proceeding with the more costly computations of a complete rocking maneuver. This work is part of an ongoing study of wing rock both with and without vortex breakdown.

2. Governing Equations

The governing equations for the present problem are the unsteady, three-dimensional, full mass-averaged Navier-Stokes equations written in strong conservation form [14] using a general, time-dependent coordinate transformation ξ, η, ζ, t:

$$\frac{\partial}{\partial t}\left(\frac{q}{J}\right) + \frac{\partial F}{\partial \xi} + \frac{\partial G}{\partial \eta} + \frac{\partial H}{\partial \zeta} = \frac{1}{Re}[\frac{\partial F_v}{\partial \xi} + \frac{\partial G_v}{\partial \eta} + \frac{\partial H_v}{\partial \zeta}] \tag{2.1}$$

where:

$$q = \begin{bmatrix} \rho \\ \rho u \\ \rho v \\ \rho w \\ \rho E_t \end{bmatrix}, \quad F = \frac{1}{J}\begin{bmatrix} \rho U \\ \rho u U + \xi_x p \\ \rho v U + \xi_y p \\ \rho w U + \xi_z p \\ \rho E_t U + p\tilde{U} \end{bmatrix}, \quad G = \frac{1}{J}\begin{bmatrix} \rho V \\ \rho u V + \eta_x p \\ \rho v V + \eta_y p \\ \rho w V + \eta_z p \\ \rho E_t V + p\tilde{V} \end{bmatrix}, \quad H = \frac{1}{J}\begin{bmatrix} \rho W \\ \rho u W + \zeta_x p \\ \rho v W + \zeta_y p \\ \rho w W + \zeta_z p \\ \rho E_t W + p\tilde{W} \end{bmatrix},$$

$$F_v = \frac{1}{J}\begin{bmatrix} 0 \\ \xi_{x_i}\tau_{i1} \\ \xi_{x_i}\tau_{i2} \\ \xi_{x_i}\tau_{i3} \\ \xi_{x_i}b_i \end{bmatrix}, \quad G_v = \frac{1}{J}\begin{bmatrix} 0 \\ \eta_{x_i}\tau_{i1} \\ \eta_{x_i}\tau_{i2} \\ \eta_{x_i}\tau_{i3} \\ \eta_{x_i}b_i \end{bmatrix}, \quad H_v = \frac{1}{J}\begin{bmatrix} 0 \\ \zeta_{x_i}\tau_{i1} \\ \zeta_{x_i}\tau_{i2} \\ \zeta_{x_i}\tau_{i3} \\ \zeta_{x_i}b_i \end{bmatrix}$$

$$U = \xi_t + \xi_x u + \xi_y v + \xi_z w = \xi_t + \tilde{U}$$

$$V = \eta_t + \eta_x u + \eta_y v + \eta_z w = \eta_t + \tilde{V}$$

$$W = \zeta_t + \zeta_x u + \zeta_y v + \zeta_z w = \zeta_t + \tilde{W}$$

$$E_t = e + \frac{1}{2}(u^2 + v^2 + w^2)$$

$$b_i = u_j\tau_{ij} + \frac{k}{(\gamma-1)PrM_\infty^2}\frac{\partial \xi_l}{\partial x_i}\frac{\partial T}{\partial \xi_l}$$

$$\tau_{ij} = \mu(\frac{\partial \xi_k}{\partial x_j}\frac{\partial u_i}{\partial \xi_k} + \frac{\partial \xi_k}{\partial x_i}\frac{\partial u_j}{\partial \xi_k}) - \frac{2}{3}\mu\delta_{ij}\frac{\partial \xi_l}{\partial x_k}\frac{\partial u_k}{\partial \xi_l}$$

$$\mu = \mu_l + \mu_t$$

$$x_1, x_2, x_3 \rightarrow x, y, z$$

$$\xi_1, \xi_2, \xi_3 \rightarrow \xi, \eta, \zeta$$

3

The system of equations is closed using the perfect gas law, Sutherland's formula for viscosity, and the assumption of a constant Prandtl number, $Pr = 0.72$. Flow quantities have been nondimensionalized by their respective free stream values except for pressure, which is nondimensionalized by twice the freestream dynamic pressure, and speed of sound which is nondimensionalized by the freestream velocity All lengths have been normalized by the root chord length of the delta wing.

3. Numerical Procedure

The governing equations are solved numerically using the implicit, approximately-factored algorithm of Beam and Warming [15]. The equations are differenced using Euler implicit time-differencing and second-order accurate central differences for all spatial derivatives. A blend of second and fourth order nonlinear dissipation, as suggested by Jameson et al. [16], is used to stabilize the central difference scheme. The current work, in which subsonic flows are investigated, requires only fourth-order dissipation. In the present numerical scheme both a full block tri-diagonal inversion scheme and a diagonalized inversion scheme based on the diagonal form of the Beam-Warming algorithm developed by Pulliam and Chaussee [17] are available.

A subiteration procedure that has been successfully used by several authors [18-20] has also been incorporated as an option in the current solution procedure [21]. The subiteration strategy provides distinct improvements to the numerical scheme. The stability limits of the three-factored algorithm are relaxed by reducing the factorization error through subiterations. This greatly improves the efficiency of the algorithm. Subiterations also provide a consistent means of implementing the diagonal form of the Beam-Warming algorithm for unsteady flows.

A fully vectorized, time-accurate code has been developed to implement the aforementioned scheme [22]. The computational requirements are 33 words/grid-point and a processing rate of 1.8×10^{-5} CPU sec/grid-point/iteration for the diagonal solver on a Cray II. The block tri-diagonal solver requires approximately twice the diagonal solver processing rate. The code has been validated for a variety of steady and unsteady flows. Both supersonic and subsonic flows over delta wings, including vortex breakdown [21,23-25] have been computed with this code. Unsteady flow simulations have been carried out for both a pitching slender body of revolution [26] and a pitching delta wing [25]. Finally, the code has been used to calculate steady and unsteady horseshoe vortex flows occurring at a cylinder/flat plate juncture [22,27]. These results have provided a broad validation base for both steady and unsteady flows.

For the body motion to be considered in this study (i.e., delta-wing roll), a general time-dependent coordinate transformation is introduced. The rigid, nondeforming grid is allowed to roll with the body and the grid motion is treated through the general coordinate transformation. This approach eliminates the need for generating multiple grids. Also, since the equations are written in an inertial frame of reference, no additional terms are required in the governing equations.

5

4. Grid Structure and Boundary Conditions

The delta-wing configuration used for the present computations corresponds to the delta-wing model used by Arena [8] in his experimental wing rock studies. The wing has an 80° leading edge sweep, a root chord of 16 5/8 in, a thickness of 1/4 in and a 45° bevel at the leading edge. In the computational configuration the trailing edge has also been beveled (9.3°) to provide for a smooth closure of the wing.

The grid chosen for the current study has an H-O structure, with O-grids being stacked axially along the delta wing (Fig. 1). This grid topology provides good resolution of the leading edge vortices and the apex region of the delta wing. The baseline grid used for these computations consists of 219 points around the body, 81 points normal to the body with a minimum spacing at the wall of $\Delta z = 0.0001$ and 89 points in the axial direction with a constant grid spacing of $\Delta x = 0.025$ over the predominant portion of the wing. The grid extends 1 chord upstream of the wing, 1.5 chords downstream of the wing and 1.5 chords in the normal direction from the wing.

The boundary conditions for the delta-wing roll problem are implemented as follows. Characteristic boundary conditions [28] are applied at the far field and upstream boundaries. At the downstream boundary first order extrapolation of the interior flow values is used. On the delta-wing surface the following conditions are applied:

$$
\vec{U} = \vec{U}_b
$$
$$
\frac{\partial T}{\partial \eta} = 0
$$
$$
\frac{\partial p}{\partial n} = -\rho \vec{a}_b \cdot \vec{n}
$$

where $\vec{U}_b$ and $\vec{a}_b$ are the velocity and acceleration of the point on the body defined as:

$$
\vec{U}_b = \vec{\omega} \times (\vec{r}_b - \vec{r}_o)
$$
$$
\vec{a}_b = \frac{d\vec{\omega}}{dt} \times (\vec{r}_b - \vec{r}_o) + \vec{\omega} \times [\vec{\omega} \times (\vec{r}_b - \vec{r}_o)]
$$

and $\vec{n}$ is the surface normal vector (see Fig. 2). For the case of roll about a fixed axis considered here, $\vec{r}_o = 0$ and $\vec{\omega} = \dot{\phi}\vec{i}$ where $\dot{\phi}$ is the roll rate.

For the H-O grid structure adopted for the present problem a singular line emanates from the apex of the delta wing and a singular line and plane are located downstream of the trailing edge. These singular surfaces are the continuation of the grid from the wing surface ahead and downstream of the delta wing.
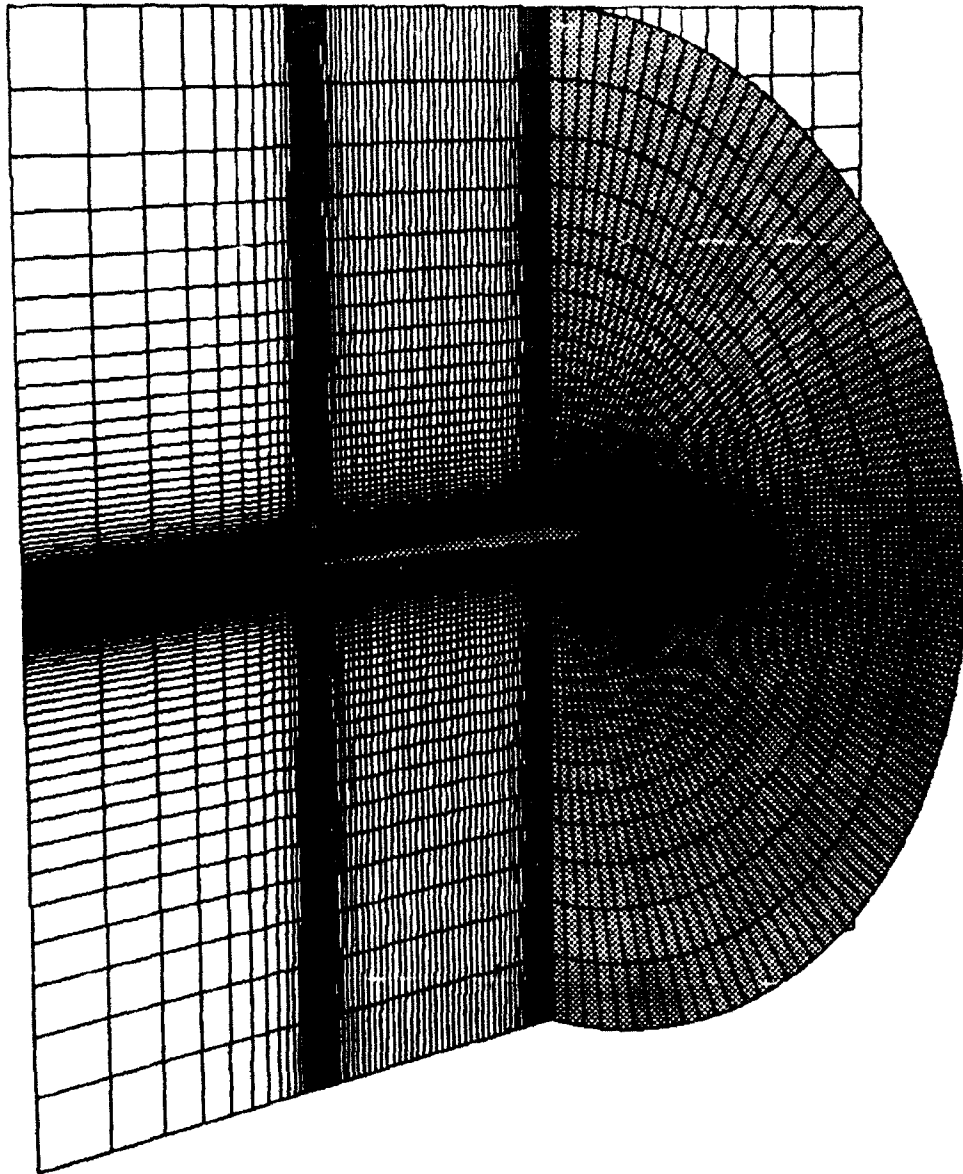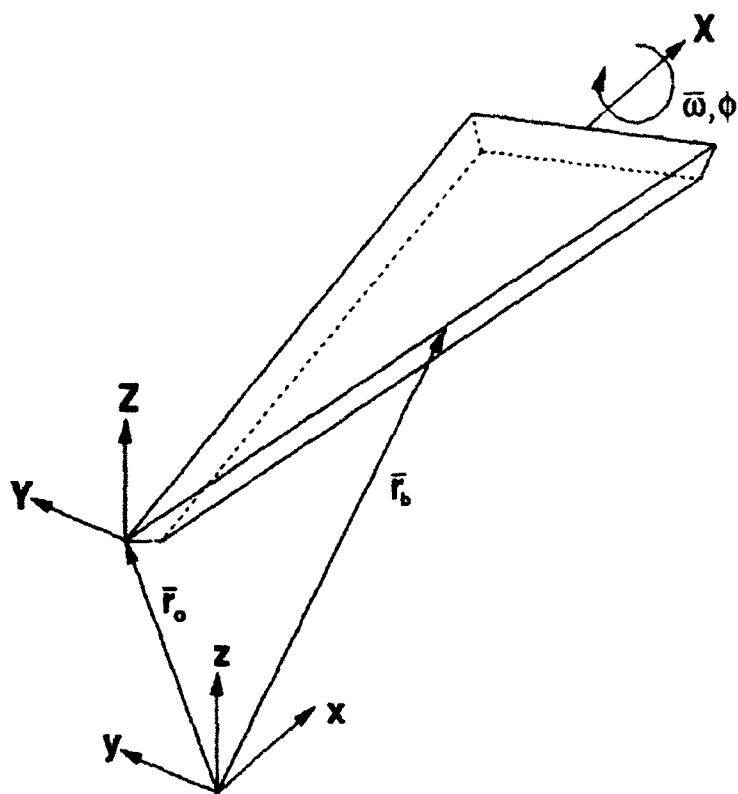
6

Figure 1: Grid Structure

Figure 2: Problem Layout

The flow variables on these surfaces are obtained by extrapolating the conserved variables to the surface and then performing the appropriate averaging of these values.

5. Results

5.1 Fixed Roll Angle

Two fixed roll angle cases ($\phi = 0°$ and $\phi = 45°$) are considered to demonstrate the capabilities of the numerical scheme before computing the dynamic roll maneuver. The flow conditions are a Reynolds number of 400,000, freestream Mach number of 0.2 and an angle of attack of 30°. These conditions correspond to the experiments of Arena [8]. These experimental measurements are used as a validation base for comparison with the present computations for rolled delta wings.

Computations for both laminar and turbulent flow cases were performed. For the turbulent flow cases the Baldwin-Lomax turbulence model [29] is used. The turbulence model has been modified similarly to Ref. [30] to account for the large vortical structures over the delta wing by restricting the search for the peak in the Baldwin-Lomax F-function to a normal distance from the body of no more than 30% of the local wing span. The flow is assumed to be turbulent over the whole extent of the wing.

The sensitivity of the solution to grid resolution and boundary location is also investigated. Computations are performed on a second grid containing $299 \times 81 \times 89$ grid points. Both the baseline grid and the refined grid have the same axial distribution of grid points with the baseline grid having 100 points and the refined grid 140 points distributed spanwise across the upper surface. The grid distribution in the body normal direction on the refined grid has been modified to enhance the resolution in the region of the vortex cores.

Figure 3 compares the computed surface pressure at several axial locations with the experimental measurements of Arena [8] for a 0° roll angle. The computed solution agrees well with the experiments, capturing all significant features observed. At $X/L = 0.9$ the minimum pressure peak is slightly under-predicted. The discrepancy in the lower surface pressure at $X/L = 0.9$ is due in part to the negative camber introduced by the lower surface trailing-edge bevel used in the computational model. Any other discrepancy between the experimental and computed pressures is well within the experimental uncertainty $\Delta C_p \approx 0.079 - 0.084$ [8]. The effect of grid boundary location on the computed solution has also been investigated for this case. The distance from the wing to all boundaries was doubled with no noticeable changes observed in the solution.

The next case considered is a delta wing at a fixed roll angle of 45°. The vortex structure over the rolled delta wing is seen in Fig. 4. The right vortex (downward leading edge) has moved inboard and towards the surface of the wing creating an extensive secondary flow region. The left vortex (upward leading edge) has
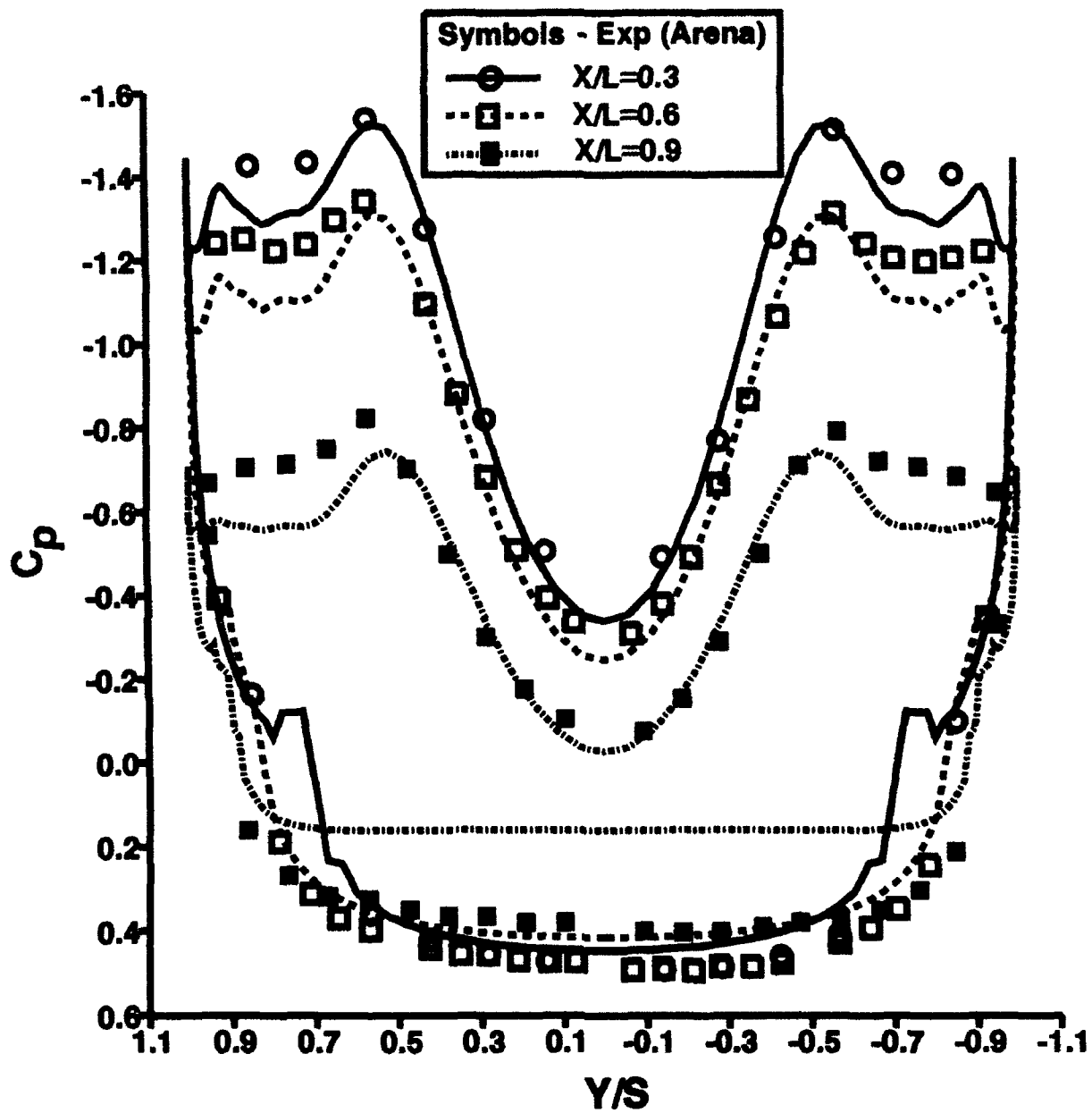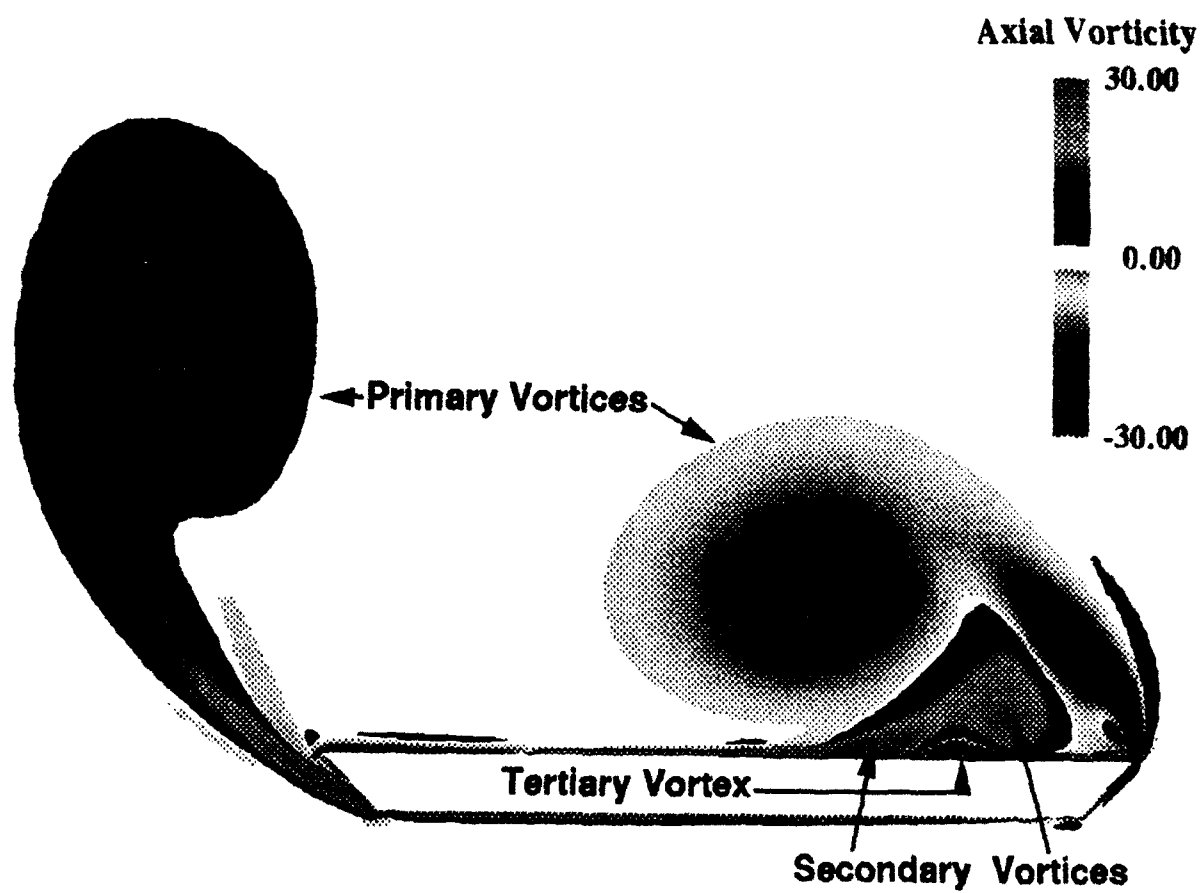
10

Figure 3: Surface Pressure Coefficient: $\phi = 0°$

11

Figure 4: Contours of the Axial Component of Vorticity: $X/L = 0.6, \phi = 45°$

moved outboard of the wing and away from the surface and its influence on the flow over the upper surface of the delta wing is greatly diminished. The shear layer that rolls up to form this vortex now separates from the lower surface bevel rather than the upward leading edge.

Figure 5 shows a comparison of the computed surface pressure at $X/L = 0.6$ for both the base grid and the refined grid with experiment [8]. Both computed solutions agree well with the experimental measurements, with only a slight overexpansion in the region under the right vortex. Improvements in the solution in this region are seen for the refined grid. Elsewhere the two solutions are virtually identical. This figure also reflects the reduction in influence of the left vortex on the surface pressure with the expansion peak due to the left vortex being eliminated.

Figure 6 compares the experimental surface oil flow with the simulated oil flow patterns for the computations on the baseline and refined meshes. Good qualitative agreement between the main features of the experimental and simulated oil flow patterns is obtained. Both the secondary and tertiary separation lines and the attachment of the downward leading edge vortex on the upper surface are captured. The curvature of the separation lines as they approach the trailing edge observed in the experiment is also seen in the computed oil flow patterns. Some differences in the aft portion of the wing between the tertiary separation line and the leading edge are seen, but the true flow topology in this region is not discernible even in the experimental oil flow picture.

Since there is not a unique relationship between the surface topology and the flow pattern above the wing, the cross-flow topology is shown in Fig. 7 at an axial location $X/L = 0.6$. In this figure features are marked as follows: S are saddle points, F are foci and N are nodes. Primed quantities denote half-saddles or nodes. The subscripts A and S denote attachment and separation, respectively. The + and - superscripts denote stable (inward spiraling) or unstable (outward spiraling) foci, respectively. This cross-flow topology satisfies the topological rule for a two-dimensional plane cutting a three-dimensional body [31] $(\sum_N + \frac{1}{2}\sum_{N'}) - (\sum_S + \frac{1}{2}\sum_{S'}) = -1$. The flow topology at this location on the delta wing differs, however, from the standard topology commonly described in the literature. No focus is associated with the left vortex which has moved outboard and away from the wing. An unstable focus with a stable limit cycle is associated with the right vortex. This cross-flow topology has also been observed for the $0°$ roll angle case. Furthermore, Visbal [25] has found limit cycle behavior in the cross-flow topology for pitching delta wings. He provides a more detailed discussion of cross-flow topology of delta wings including the occurrence of limit cycles and stable and unstable foci. In the secondary and tertiary flow regions, all the foci are unstable foci. The stable focus located above the delta wing and near the leading edge is associated with the accumulation of vorticity in the shear layer emanating from the leading edge of the
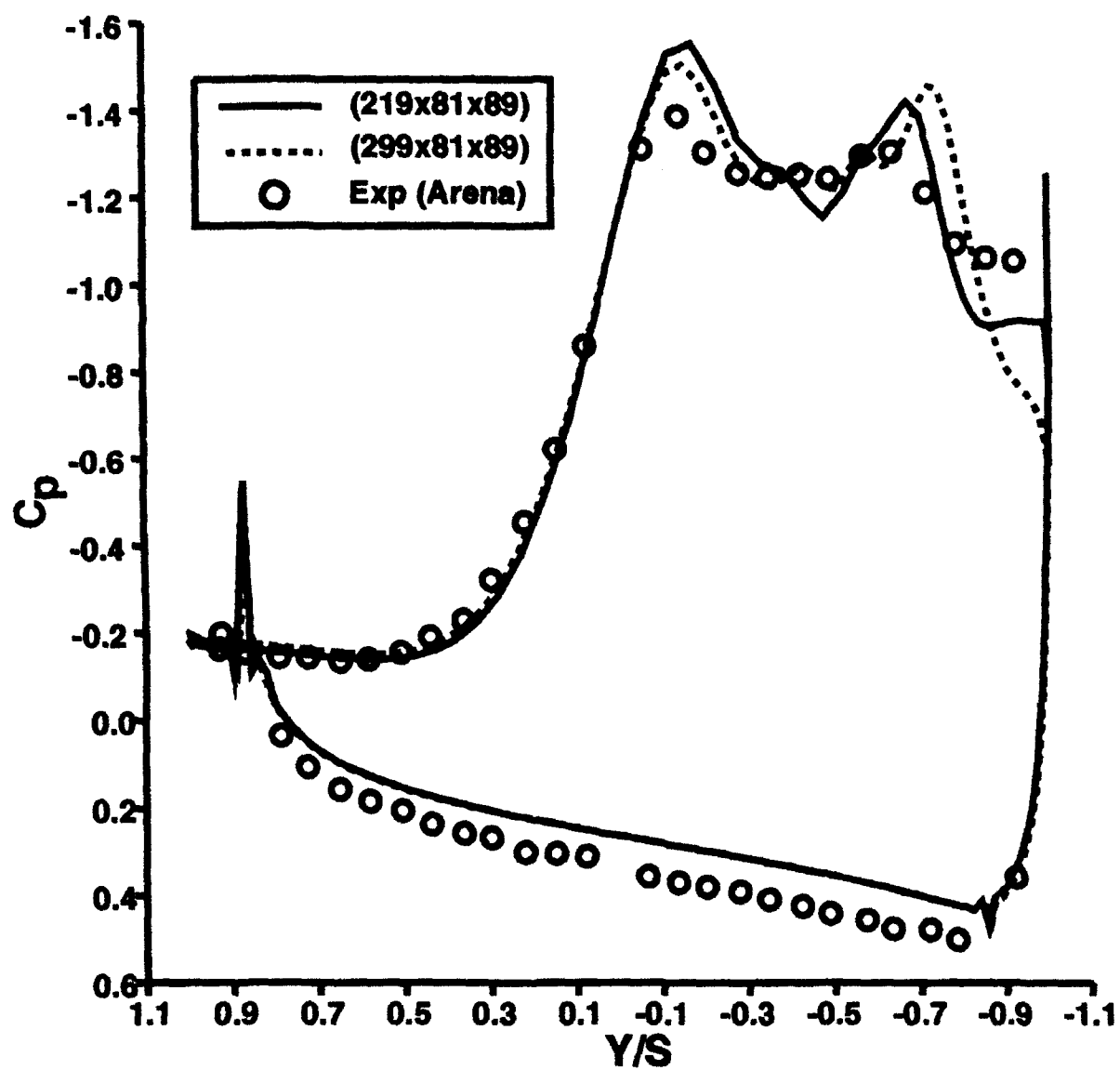
13
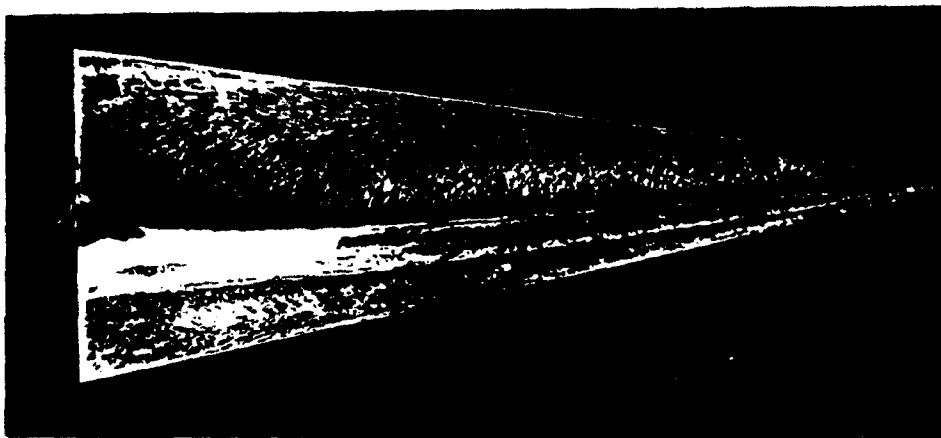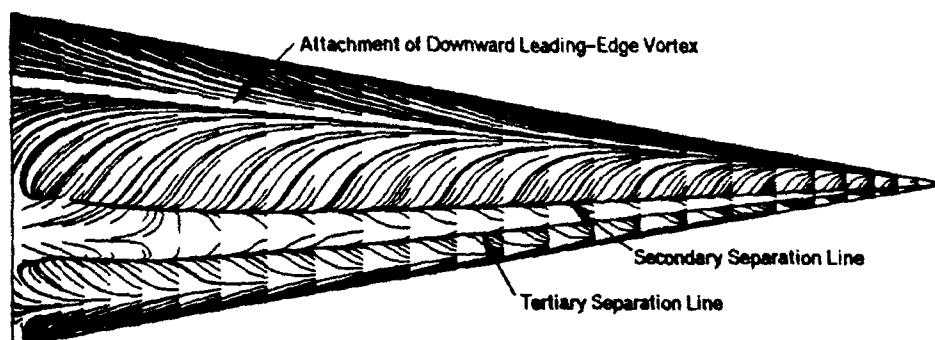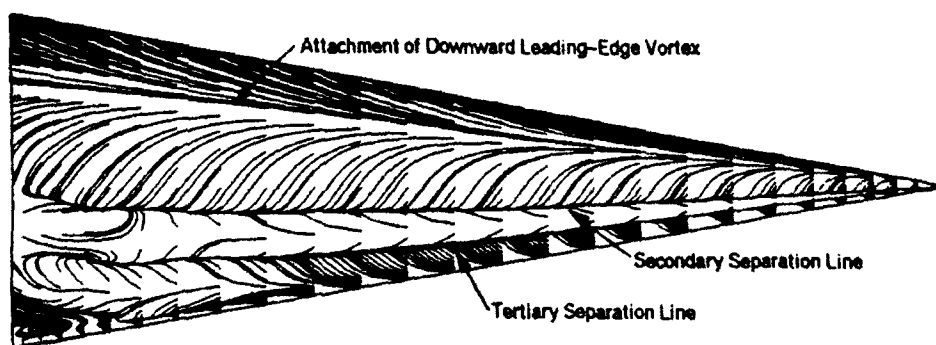
Figure 5: Surface Pressure Coefficient: $X/L = 0.6$, $\phi = 45°$

a) Experiment (Arena)

b) Baseline Grid

c) Refined Grid

Figure 6: Surface Oil Flow:a) Experiment [8], b) Baseline Grid, c) Refined Grid
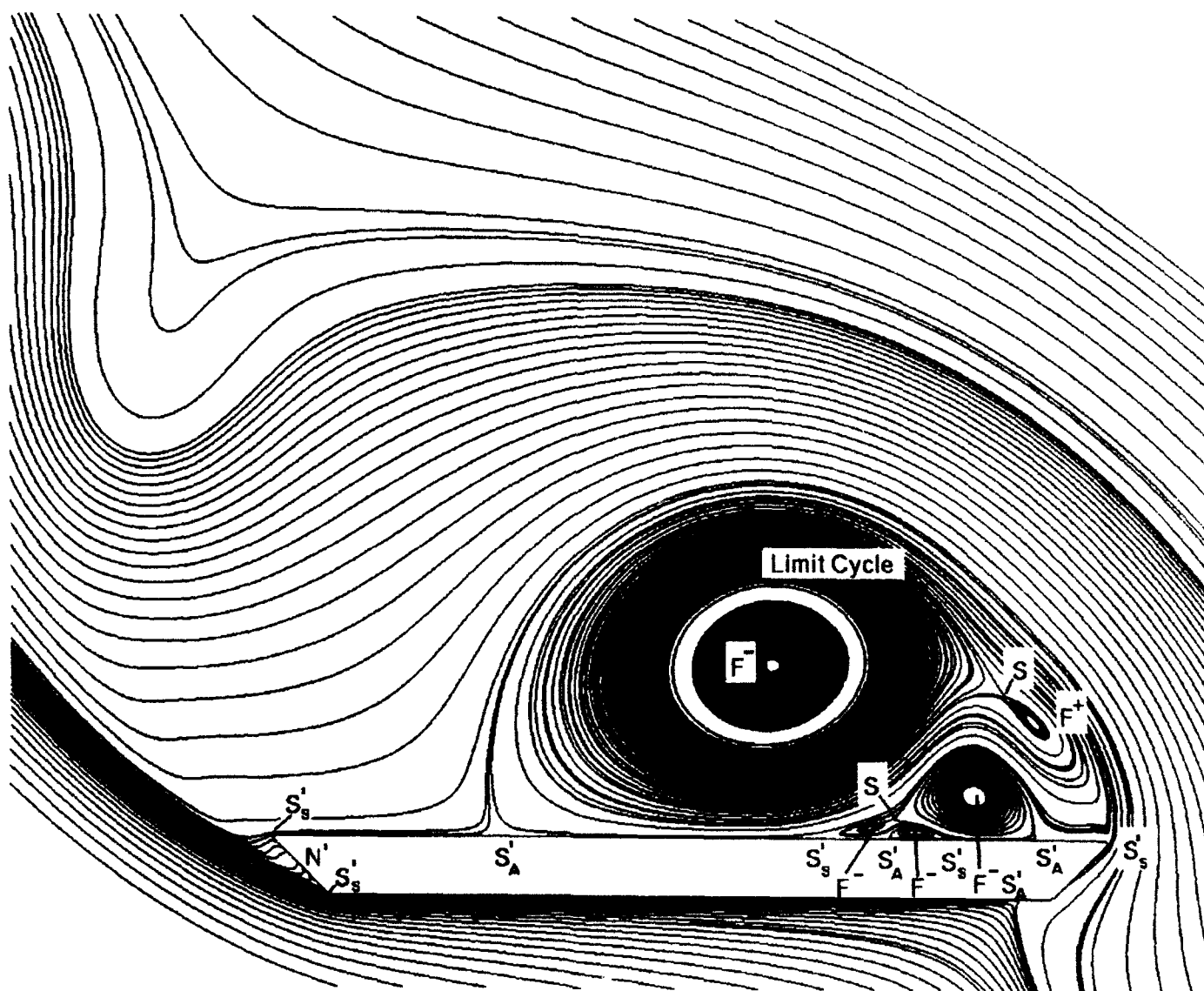
15

Figure 7: Cross-Flow Topology above the Wing, $X/L = 0.6$

Table 5.1: Vortex Core Locations at $x = 0.6$

Case		Laminar	Laminar	Turbulent	Turbulent	Experiment
		$219 \times 81 \times 89$	$299 \times 81 \times 89$	$219 \times 81 \times 89$	$299 \times 81 \times 89$	Ref. [8]
$\phi = 0°$	y	0.613	*****	0.637	*****	0.652
	z	0.489	*****	0.489	*****	0.484
$\phi = 45°$	y	-0.220	-0.225	-0.249	-0.249	-0.259
Right	z	0.402	0.417	0.402	0.402	0.450
$\phi = 45°$	y	1.380	1.370	1.399	1.409	1.387
Left	z	0.939	0.968	0.997	1.025	0.994

delta wing (see Fig. 4).

Turbulent flow solutions have also been computed for roll angles of 0° and 45°. Figure 8 compares the computed surface pressure coefficients for turbulent flow with the laminar flow results and the experimental measurements for the 45° roll case. The turbulent flow solution shows a higher suction under the primary vortex and a reduction in the influence of the secondary flow. This behavior of the surface pressure is consistent with the experimental measurements of Hummel [32] for a 76° sweep delta wing at 0° roll angle where the boundary layer was artificially tripped halfway between the leading edge and the centerline of the wing. The comparison with the experiments of Arena [8] also further confirms that the experimental flow is laminar.

Table 5.1 gives a comparison of the computed vortex core locations with the experimental core locations at $X/L = 0.6$. The experimental measurements are subject to an uncertainty of ±0.083. The vortex core locations for all cases lie well within the experimental error range. The turbulent vortex cores are further outboard of the corresponding laminar flow core locations. This is due to the reduced size of the secondary vortex for turbulent flows.

5.2 Dynamic Roll Maneuver

Figure 9 shows the roll maneuver to be computed. The maneuver consists of a constant rate roll from 0° to 45° with a smooth acceleration and deceleration. The nondimensional roll rate is $\Phi = 0.1325$. This is the mean roll rate for one cycle in the wing-rock experiments of Arena [8]. Since no experimental data exist for this maneuver, the computations were run for a much lower Reynolds number than the static cases,
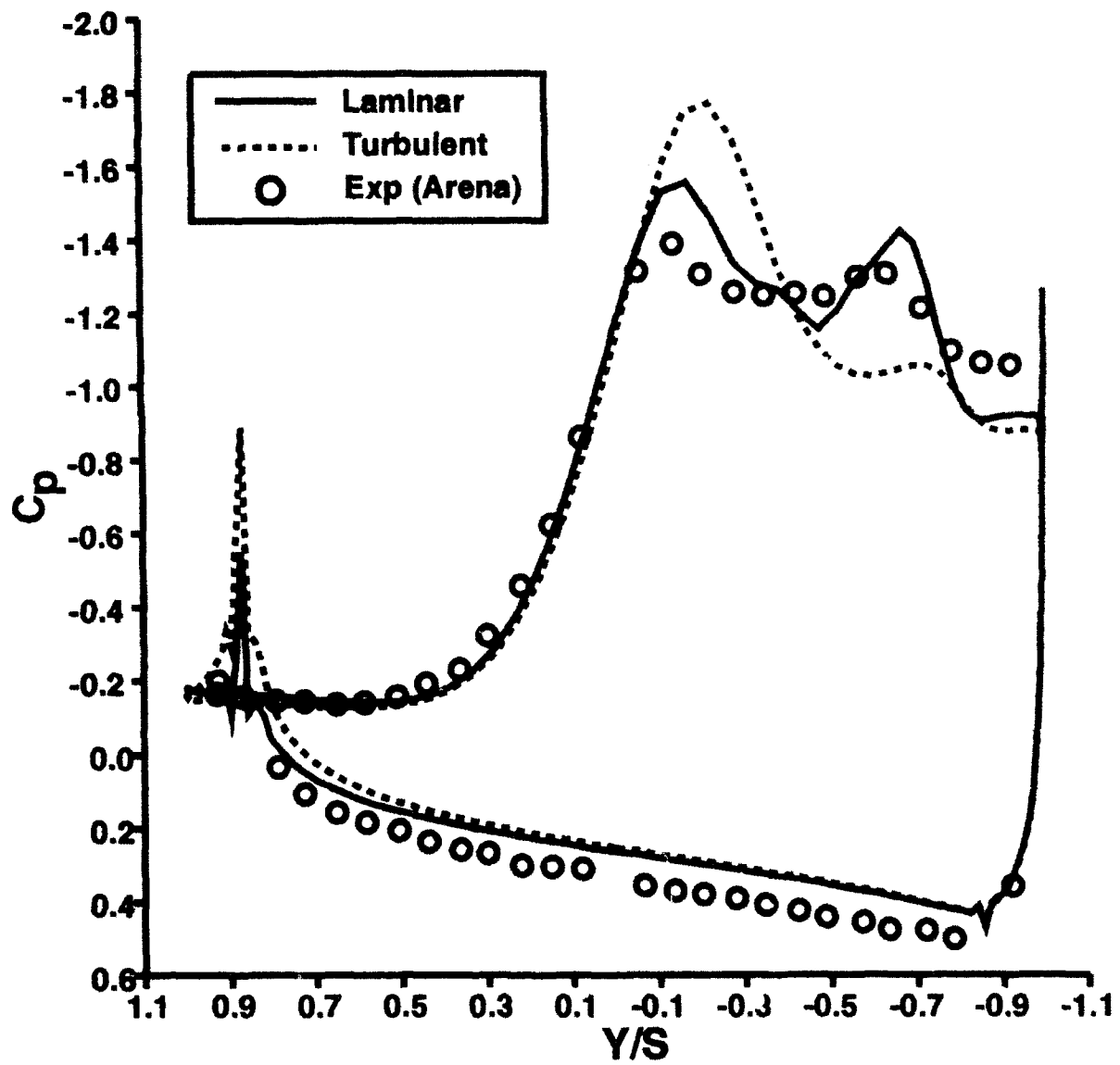
17

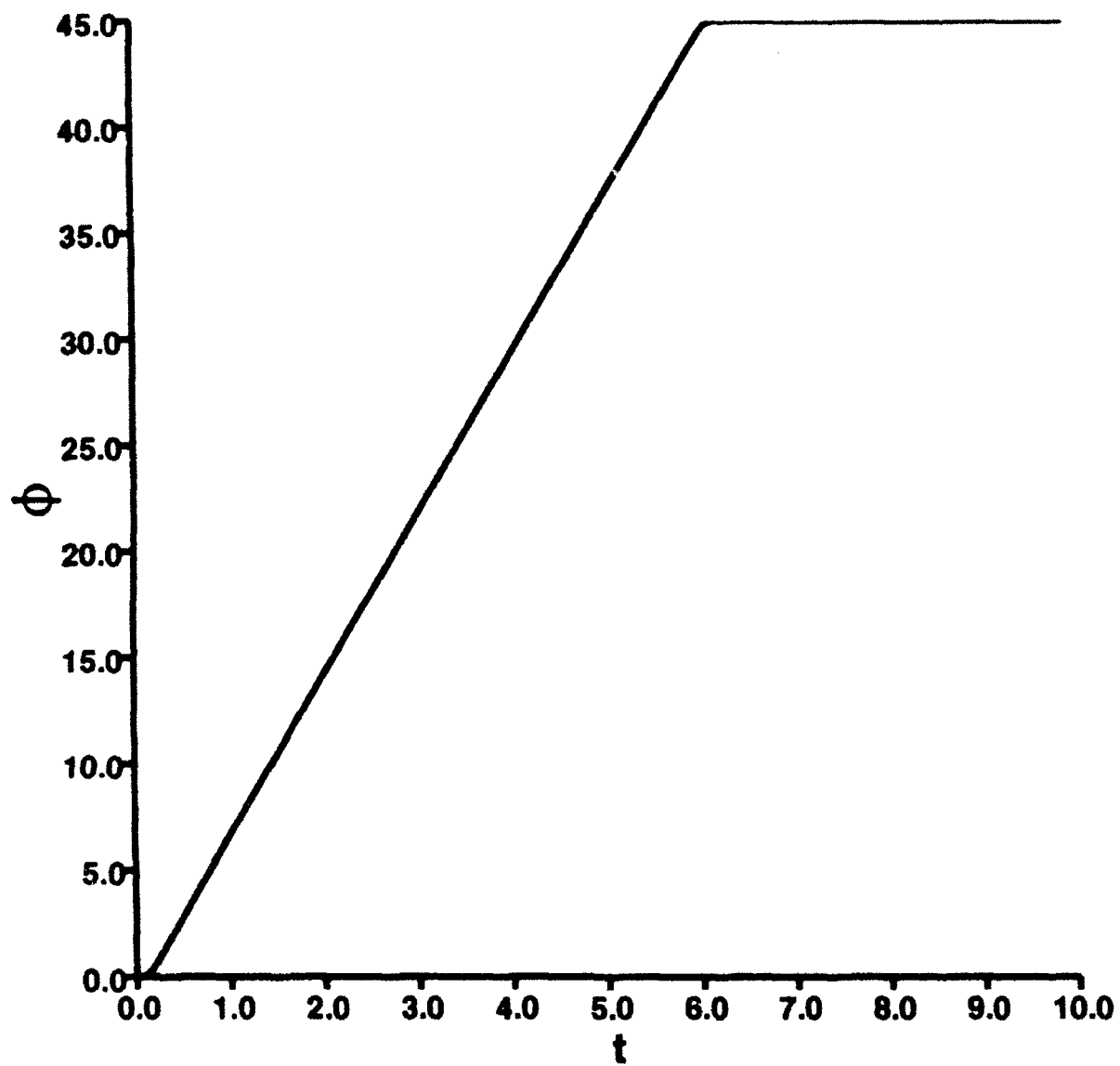Figure 8: Surface Pressure Coefficient $X/L = 0.6$, $\phi = 45°$

Figure 9: Delta Wing Roll Maneuver

$Re = 10,000$. This provides the most confidence in the computed results by eliminating any questions of turbulence, transition, or the susceptibility to and effect of shear-layer instabilities [21]. Furthermore, computing at lower Reynolds numbers provides improved grid resolution for the same number of grid points.

Figures 10 and 11 present the effects of lower Reynolds number on the flow for $\phi = 45^\circ$ roll angle. Figure 10 indicates the effect on the surface pressure at $X/L = 0.6$. Only a very small effect is seen on the lower surface. On the upper surface, the lower Reynolds number case has significantly less expansion under the right vortex. The peak minimum pressure for the lower Reynolds number case also occurs inboard of the peak for the nigher Reynolds number case. These differences in the surface pressure may be attributed to two causes. The right vortex is stronger for the higher Reynolds number, $C_{p_{core}} = -3.96$, than for the lower Reynolds number, $C_{p_{core}} = -1.86$. The second cause is a difference in the secondary flow features. Figure 11 may be compared with Fig. 6 to determine the effect of lower Reynolds number on the surface oilflow pattern. Distinct differences are observed in the secondary flow region with the lower Reynolds number case showing no tertiary separation. Examination of the cross- flow topology revealed that one large secondary vortical structure exists for the low Reynolds number case. This larger secondary vortex causes the right vortex to be located further inboard thus shifting the peak in minimum pressure. The low Reynolds number case also has a more extensive reverse flow region towards the trailing edge. Even with the differences that have been noted, the low Reynolds number computations for a forced rolling motion should provide valuable insight into the overall dynamics and behavior of the primary leading edge vortices.

The computation of the roll maneuver for the delta wing is very costly, requiring approximately 225 CPU hours on a Cray II. In order to minimize the computing time required, the diagonal form of the algorithm is used with two subiterations. The subiterations reduce the effect of the temporal errors introduced in the diagonalization process. This technique for computing unsteady flow fields due to dynamic motion has been compared with the use of a fully time accurate block tri-diagonal solver for the problem of 2-D dynamic stall. A comparison (not included) up to and through the formation of the dynamic stall vortex showed virtually no difference in the two solutions. The time step used for the unsteady computation is $\Delta t = 0.001$.

The thin-layer Navier-Stokes equations are also solved in order to reduce the computation time. Webster and Shang [23] have shown that the thin-layer and full Navier-Stokes equations give nearly identical solutions for delta wings at modest angles of attack. For the case of a dynamic motion, Stanek and Visbal [26] have shown that no appreciable difference exists between the thin-layer and full Navier-Stokes solutions for a pitching ogive. In the present computations the viscous effects are properly resolved in

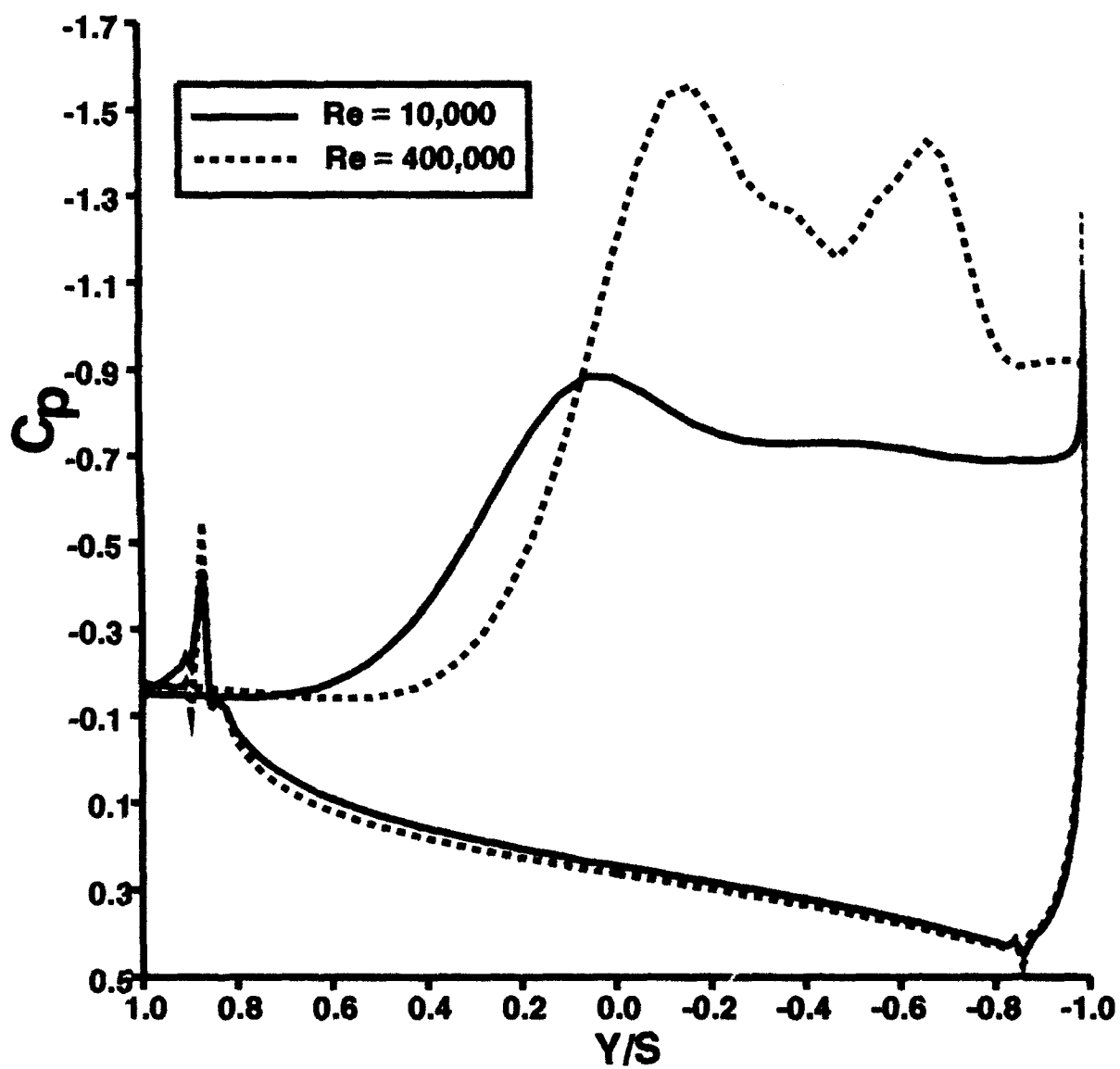Figure 10: Comparison of Surface Pressure Coefficient for Two Reynolds Numbers: $X/L = 0.6$, $\phi = 45°$

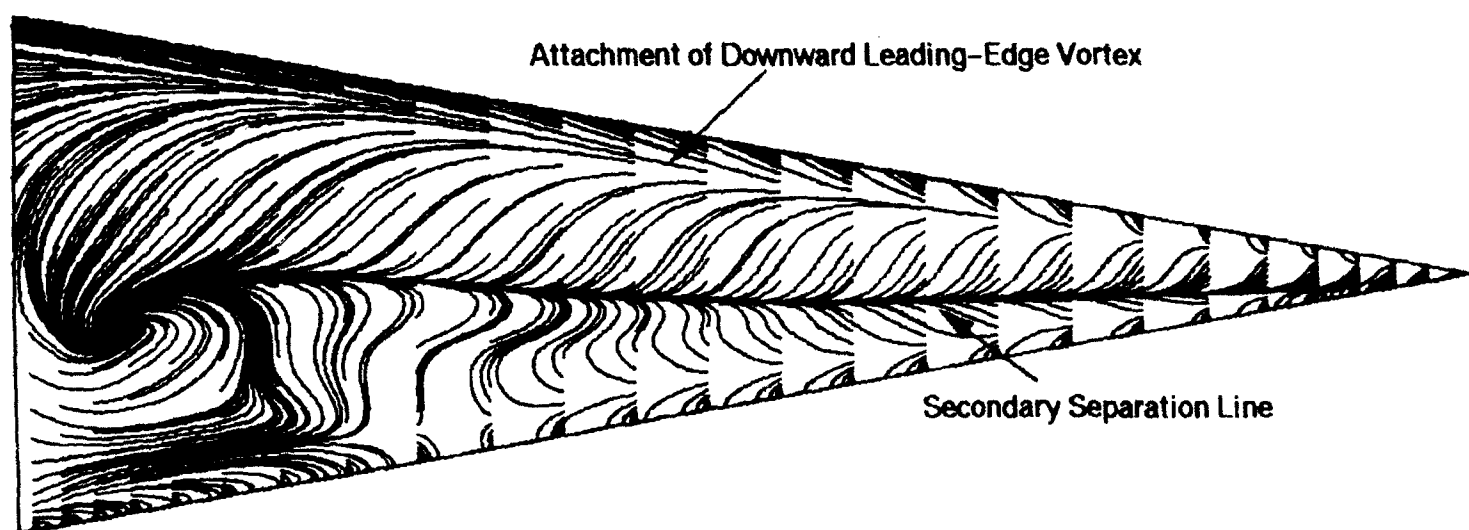**Attachment of Downward Leading-Edge Vortex**

Secondary Separation Line

Figure 11: Surface Oil Flow: $Re = 10,000$, $\phi = 45°$

regions near the wing and where the shear layer that feeds the primary vortices is formed. In both these regions the thin-layer approximation retains the relevant viscous terms.

Figure 12 shows the typical behavior of the vortices in a cross-flow plane during the rolling motion. Contours of the axial component of vorticity at $X/L = 0.9$ are shown for various roll angles during the maneuver. Also included in this figure is the corresponding surface pressure coefficient at $X/L = 0.9$. The vorticity contours show the general dynamic behavior of the vortices during the roll maneuver. As the wing rolls, the right vortex (downward leading edge) moves inboard on the wing and towards the surface. The left vortex moves outboard of the wing and away from the surface. Up to approximately $\phi = 30°$ the right vortex moves inboard and towards the wing and the secondary flow region underneath the right vortex grows in size. Subsequently, the secondary flow region is forced towards the wall and diminishes in size. When the wing stops, a new secondary flow region emerges with the predominant portion being well inboard of the leading edge. As the left vortex moves outboard and away from the surface, the secondary flow associated with this vortex decreases in strength and eventually disappears.

The actual motion of the vortex cores is plotted in Fig. 13. The vortex core location was defined as the point of minimum pressure in the core region. After the initial acceleration, the vortices move in basically a linear fashion until the wing stops. When the wing stops, the left vortex shows a rapid increase in the Z (body normal) direction to its final position. This time lag in the normal position of the left vortex core is similar to the lag observed by Arena and Nelson [33] for the vortex coming from the upward moving edge of a rocking delta wing. The change in position of the right vortex after the wing stops is mainly attributable to the reemergence of the secondary flow region.

An indication of the vortex strength may be obtained by examining the minimum pressure in the vortex core. Figure 14 gives the variation of the strength of the vortex cores as the wing rolls by plotting the minimum pressure coefficient in each core at $X/L = 0.9$. Up to $t \approx 2.0$ ($\phi \approx 14.6°$) the strength of the right vortex increases. After this time the strength drops off until $t \approx 7.45$ (1.275 characteristic times after the wing stops) where the strength levels off to its final value. The left vortex consistently loses strength until $t \approx 7.15$. Similar behavior is observed if either the maximum total pressure loss or axial (u) velocity in the core is used as indication of the vortex strength.

The behavior of the vortices during the roll maneuver may be simply understood by considering the effective angle of attack and sideslip angle (or alternatively the effective sweep angle) during a roll maneuver. From purely trigonometric considerations (no roll motion considered) the effective angle of attack and the effective sideslip angle are given by:
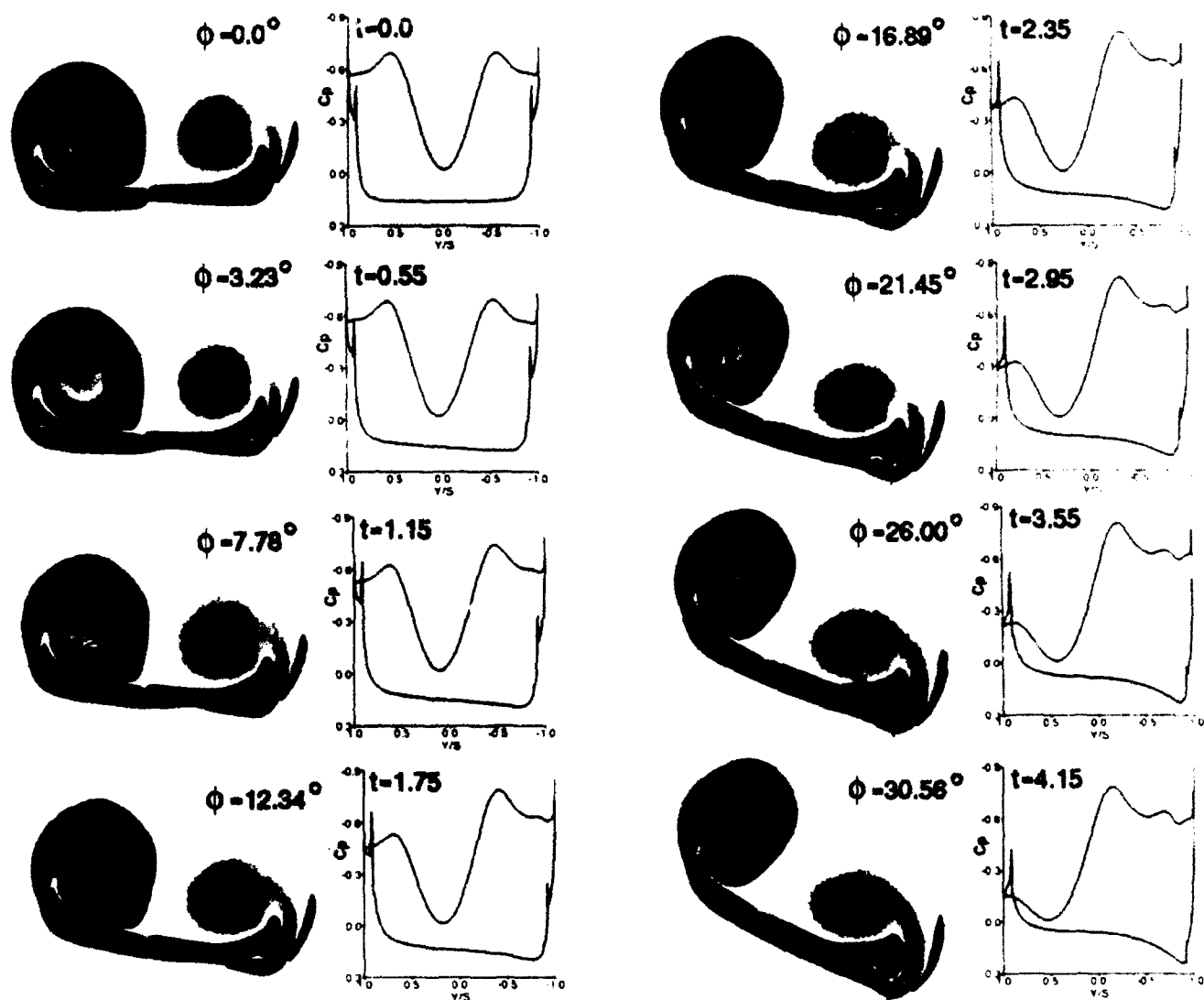
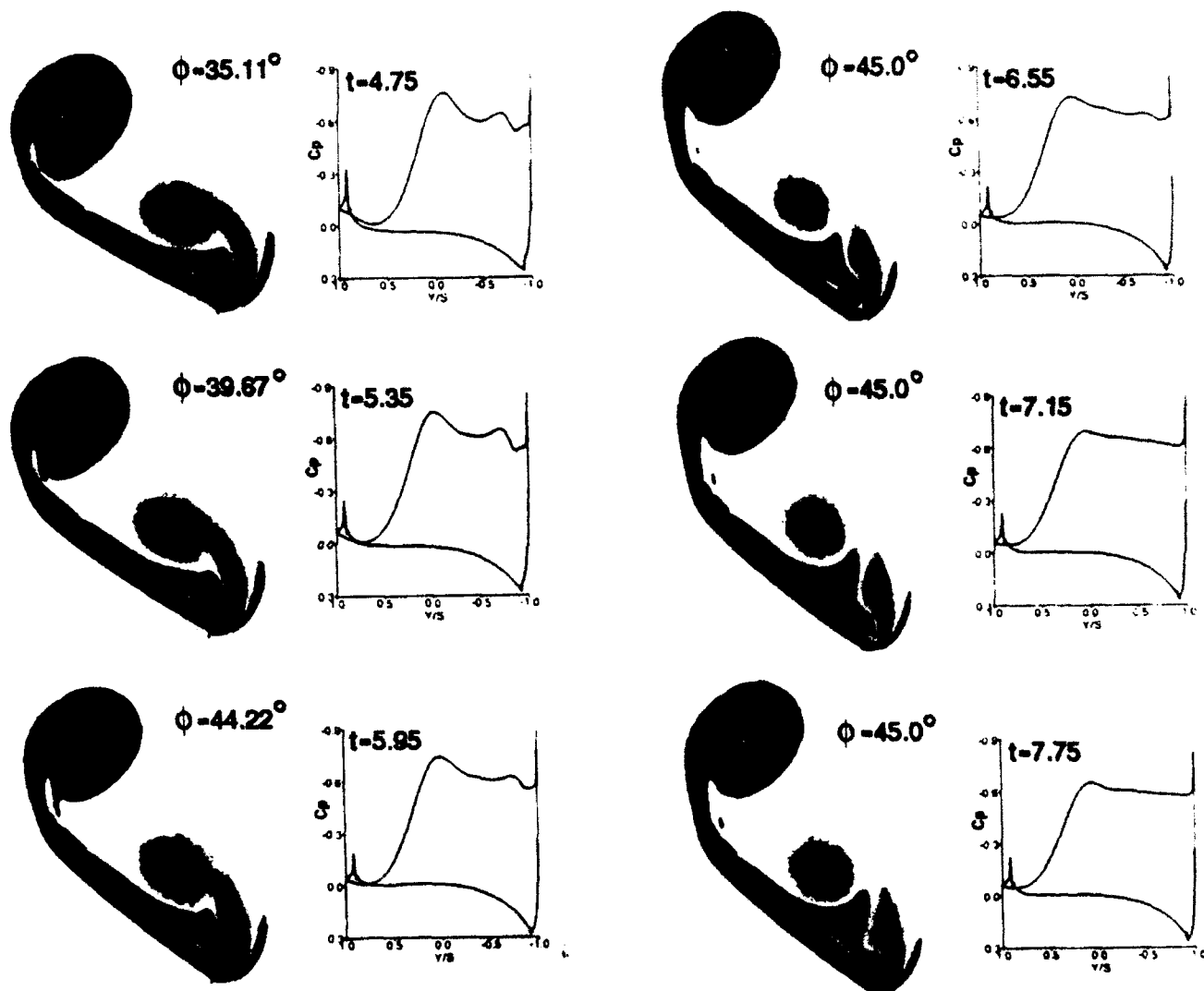Figure 12: Vortex Dynamics during the Roll Maneuver: $X/L = 0.9$

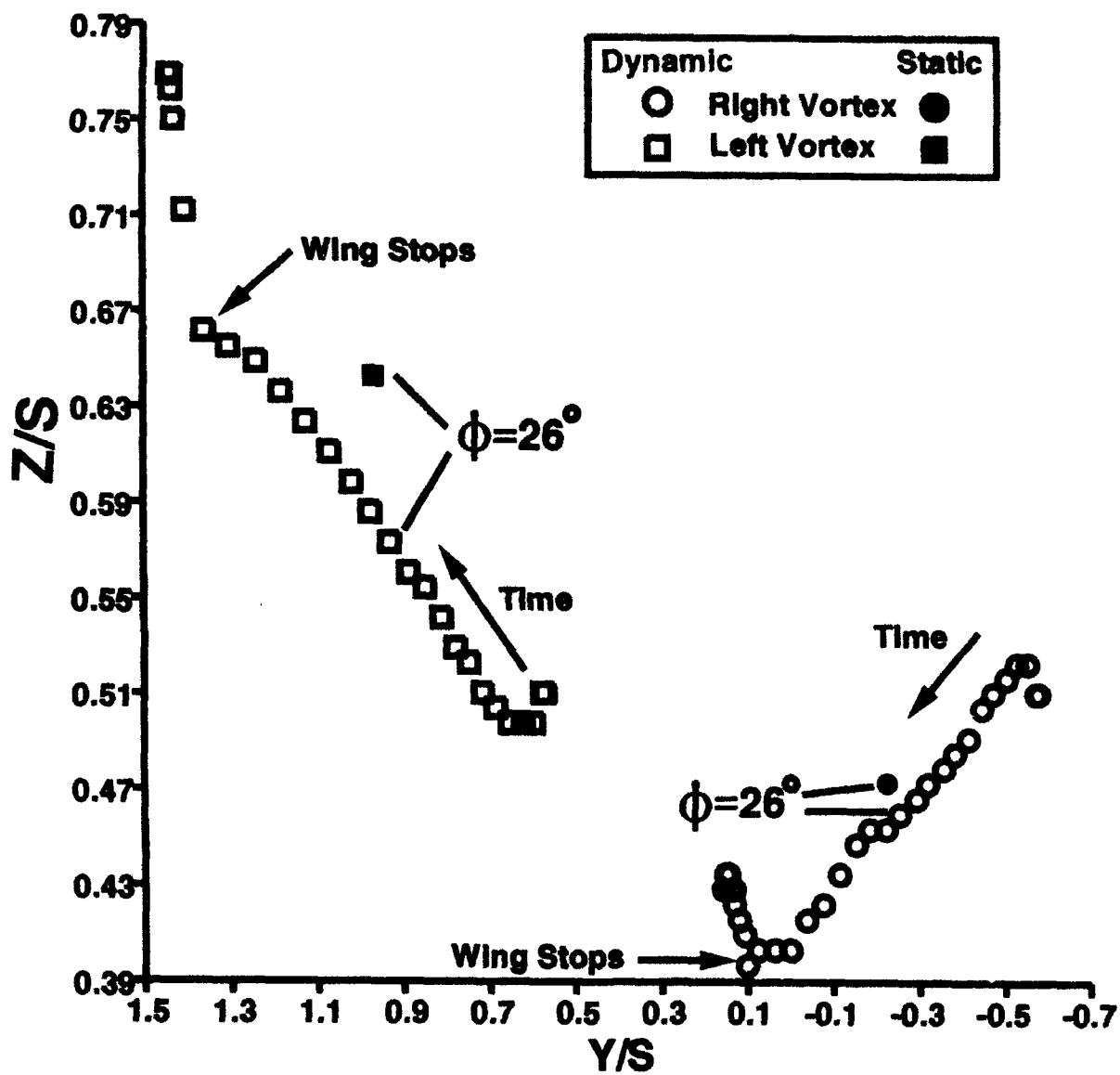Figure 12: Vortex Dynamics during the Roll Maneuver:$X/L = 0.9$ (cont'd)
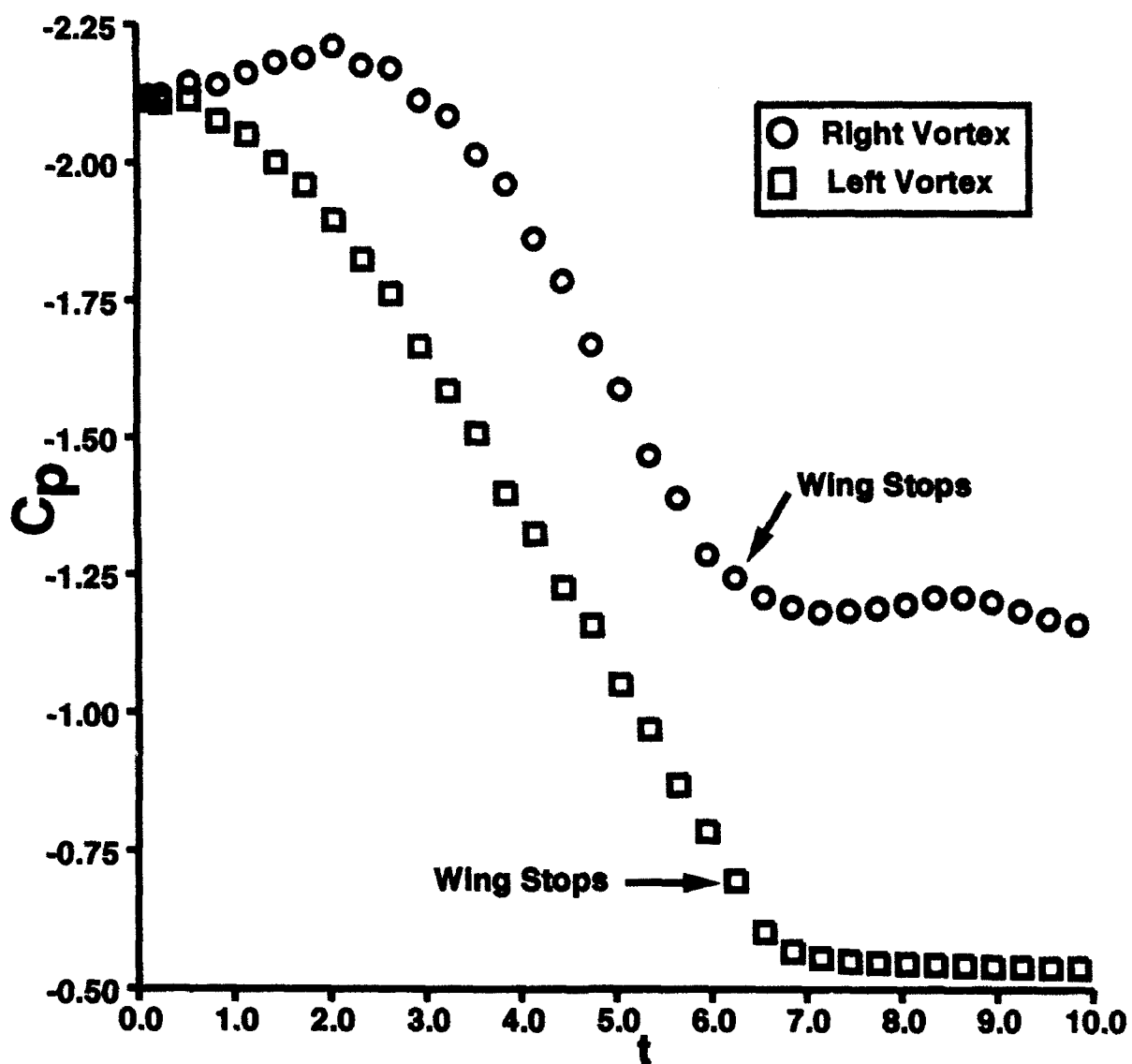
Figure 13: Core Location Motion at $X/L = 0.9$

Figure 14: Vortex Strength during Roll at $X/L = 0.9$

$$\alpha_{eff} = tan^{-1}(tan\alpha cos\phi) \qquad\qquad (5.1)$$

$$\beta_{eff} = sin^{-1}(sin\alpha sin\phi) \qquad\qquad (5.2)$$

Figure 15 shows α_{eff} and β_{eff} for the 30° angle of attack case being considered. Veerhaagen and Naarding [34] have shown that for delta wings the windward leading edge vortex moves inward and closer to the surface of the wing while the leeward vortex moves outward and away from the wing for increasing sideslip. This is consistent with the vortex motion observed for the rolling delta wing. Veerhagen and Naarding also show that as the sideslip is increased the strength of the windward vortex increases while the stre. gth of the leeward vortex decreases. Furthermore, it is known that the strength of the vortices over a delta wing decreases with decreasing angle of attack. Using these observations and Fig. 15, the behavior of the strength of the vortices during the roll maneuver may be explained. The rolling of the delta wing leads to a reduction in the effective angle of attack and a positive sideslip angle. The net effect on the left vortex (leeward) is a continuous reduction in the strength of the vortex as seen in Fig. 14. Figure 15 shows that for small roll angles (up to approximately 20°) the effective angle of attack reduces very slowly while the effective sideslip angle increases rapidly. As higher roll angles are achieved the effective angle of attack drops much more rapidly. This leads to an initial increase in the strength of the right vortex as the wing rolls to approximately 17° since the effect of increasing sideslip dominates. After a roll angle of approximately 22° the strength of the right vortex starts to rapidly drop as the effect of the reduction in effective angle of attack increases and the increase in the strength of the vortex due to increasing sideslip levels off.

The effect on the surface pressure of the variation in vortex position and strength can be seen by referring to Fig. 12. The behavior of the surface pressure at $X/L = 0.9$ is typical of other cross-plane locations. As the delta wing rolls, the large expansion due to the left vortex continually drops as the influence of this vortex on the surface is reduced and it reduces in strength. The expansion peak due to the right vortex initially moves inboard and grows until $t = 2.65$ ($\phi = 19.2°$) where the value of this peak then starts to diminish. This correlates with the point where the right vortex starts to rapidly lose strength due to the roll angle. During the roll maneuver the expansion region due to the right vortex covers a growing portion of the wing as this vortex moves inboard.

The effect of the variation in surface pressure on the lift and roll moment coefficients is seen in Figs. 16 and 17. Figure 16 shows that the lift coefficient drops rapidly as the wing rolls, dropping by 44% of its original value when the wing stops. The tilting of the normal force vector as the wing rolls provides a significant portion of the loss in lift. The behavior of the roll moment coefficient during the roll maneuver
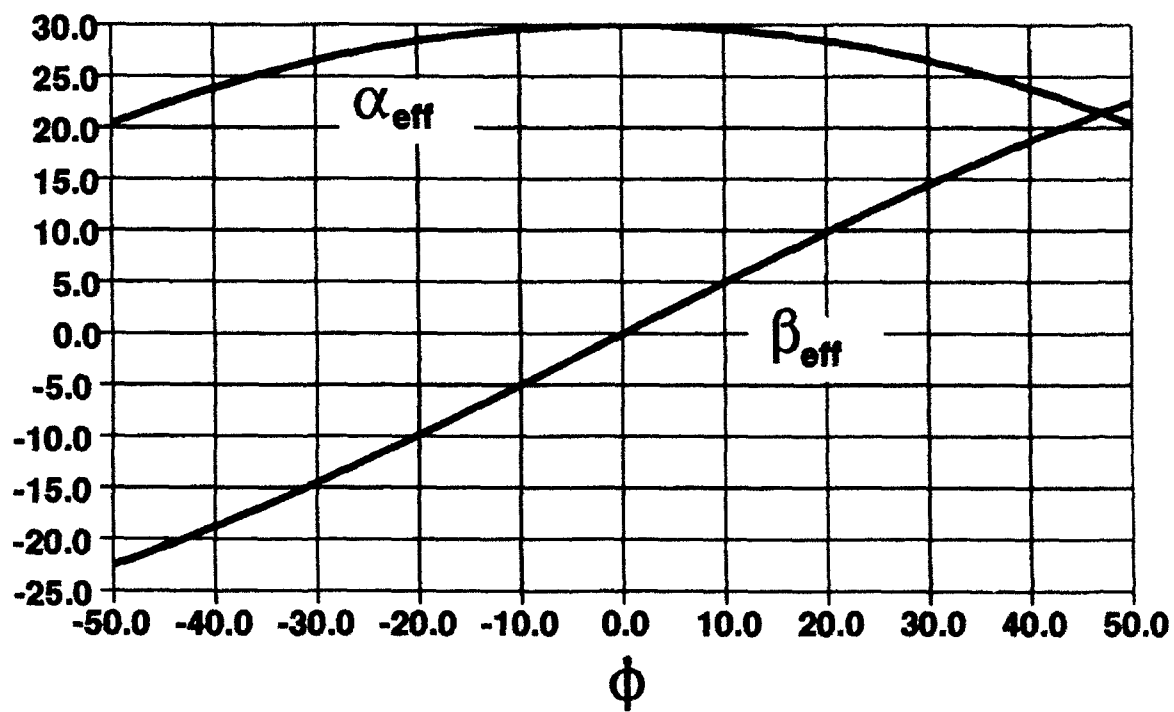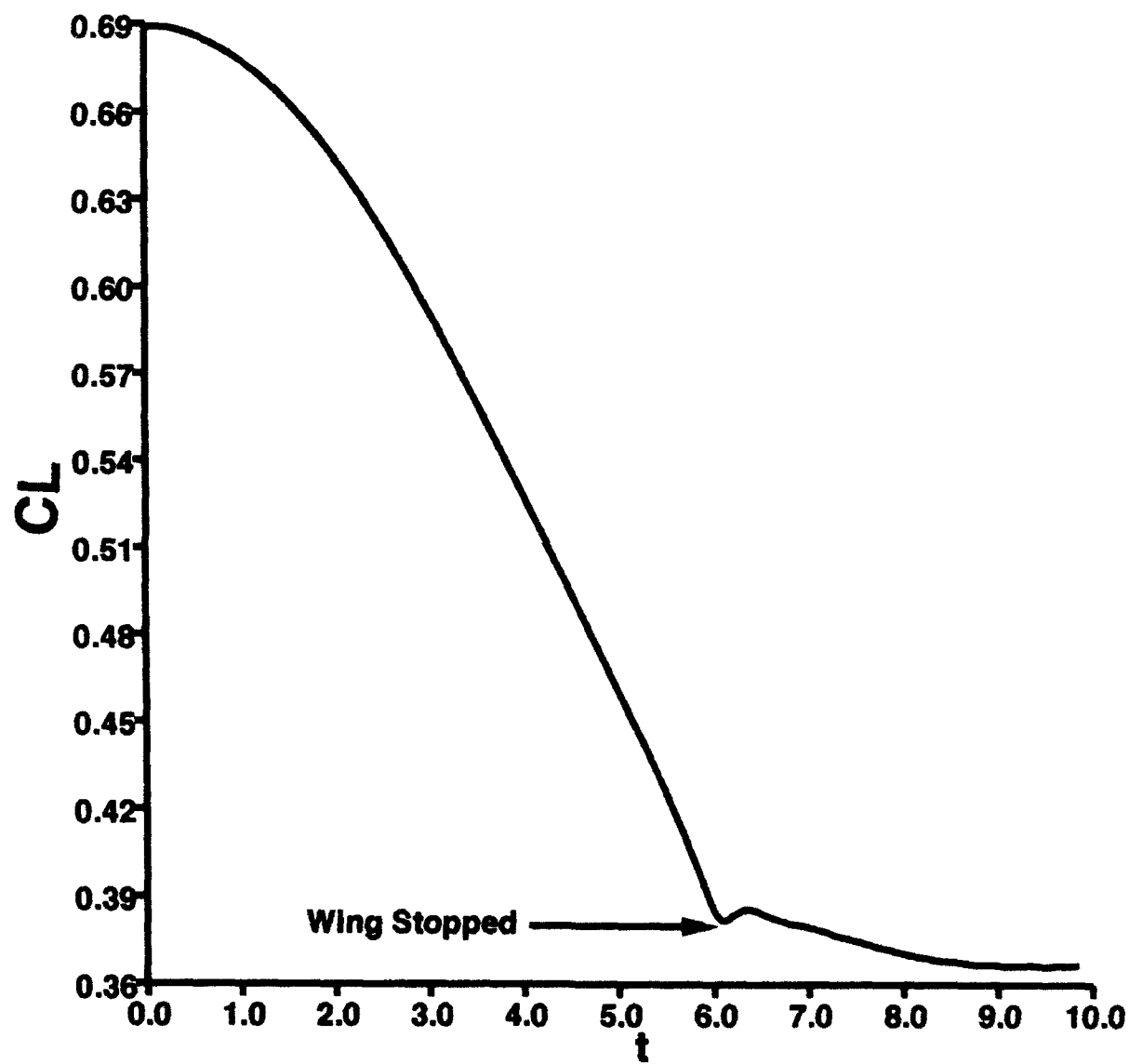
28

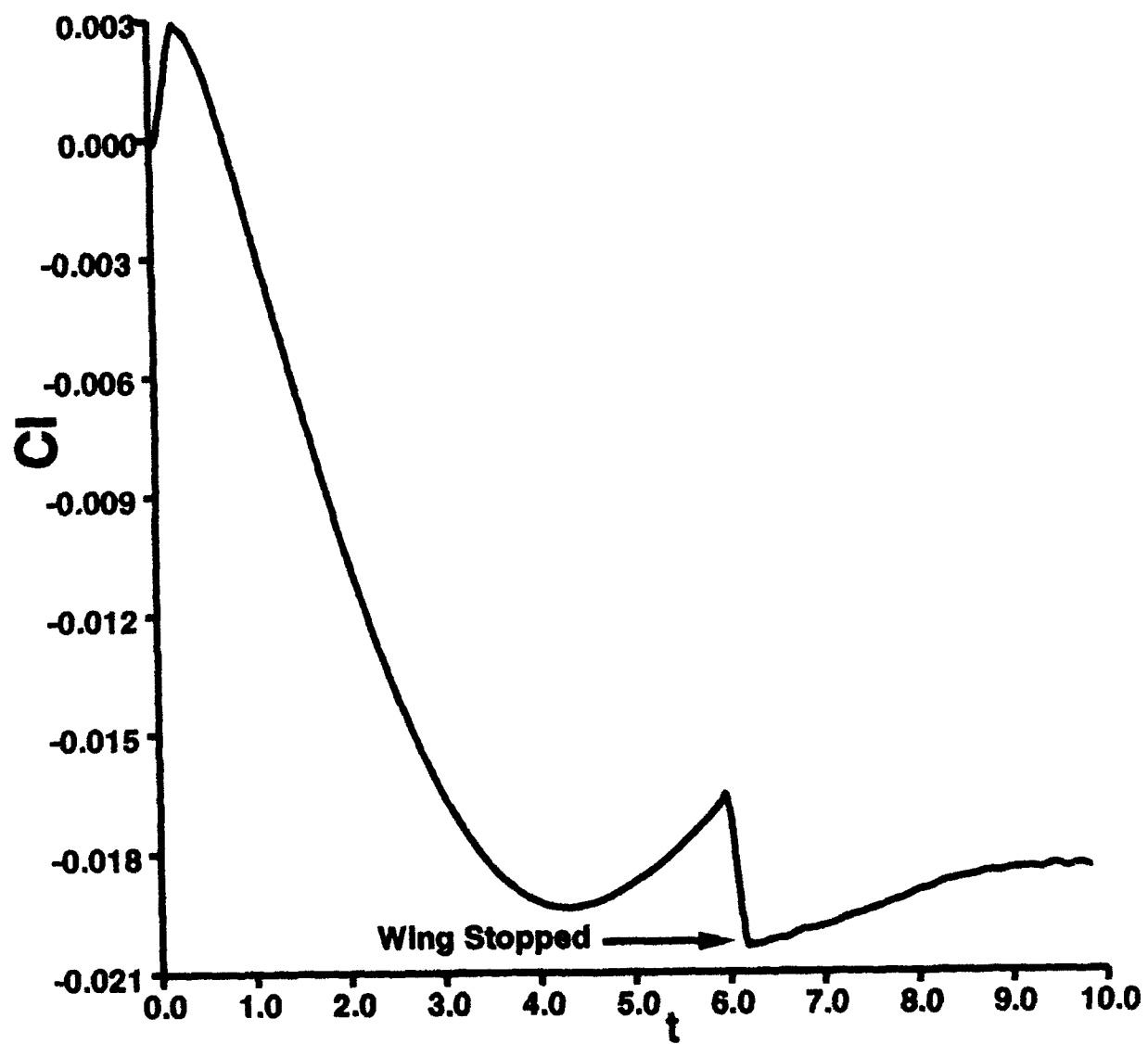Figure 15: Effective Angle of Attack and Sideslip

Figure 16: Lift Coefficient

30

Figure 17: Roll Moment Coefficient

Table 5.2: Comparison of Dynamic and Static Parameters: $X/L = 0.5$, $\phi = 26°$

		Y/S	Z/S	$C_{p_{core}}$	CL	Cl
Right	Static	-0.221	0.473	-1.717	0.551	-0.0218
Vortex	Dynamic	-0.252	0.460	-2.015	0.557	-0.0185
Left	Static	0.970	0.643	-1.237		
Vortex	Dynamic	0.933	0.573	-1.508		

is seen in Fig. 17. The initial acceleration of the wing creates a sharp rise in the roll moment. As the wing rolls at a constant rate the roll moment decreases until it reaches a minimum, $Cl = -0.0194$ at $t \approx 4.28$ ($\phi = 31.55°$). The roll moment then increases until it drops sharply when the wing decelerates to a stop. This effect on the roll moment coefficient can be explained by considering the surface pressure, Fig. 12. During the initial part of the roll, the development of the roll moment is dominated by the decrease of the favorable roll moment due to the left vortex and the increase in the opposing moment due to the right vortex. As the wing approaches and rolls through the 30° roll angle, the favorable roll moment from the left vortex has reached a minimum and the opposing moment from the right vortex has started to level off. The right vortex has now moved significantly inboard and starts to influence the pressure on the left-half of the wing, enhancing the favorable roll moment from this half of the wing. This combination leads to the development of the minimum in the roll moment coefficient.

Both the lift coefficient and roll moment coefficient show long relaxation times to attain their final values, approximately 3.0 characteristic times. Both primary vortices have achieved their final strength and position by 1.3 characteristic times after the wing motion has stopped. The additional relaxation time required for the lift and roll moment is mainly attributable to the time required for the secondary flow to establish itself after the wing stops. The low Reynolds number for these computations enhances this secondary flow effect.

Finally, the dynamic and static data are compared for a roll angle $\phi = 26°$ to ascertain dynamic effects. Table 5.2 compares the vortex locations, vortex strength, lift coefficient and roll moment coefficient. The dynamic location of the right vortex is outboard and closer to the wing than the static location. The dynamic location of the left vortex is inboard and closer to the wing than the static location. (See also Fig. 13.) The vortex strength is greater for the dynamic vortices. Figure 18 shows the corresponding effect on the surface pressure. Only a small dynamic effect is seen on the lower surface with a more significant effect apparent on the upper surface pressures. The difference in the upper surface pressure distribution
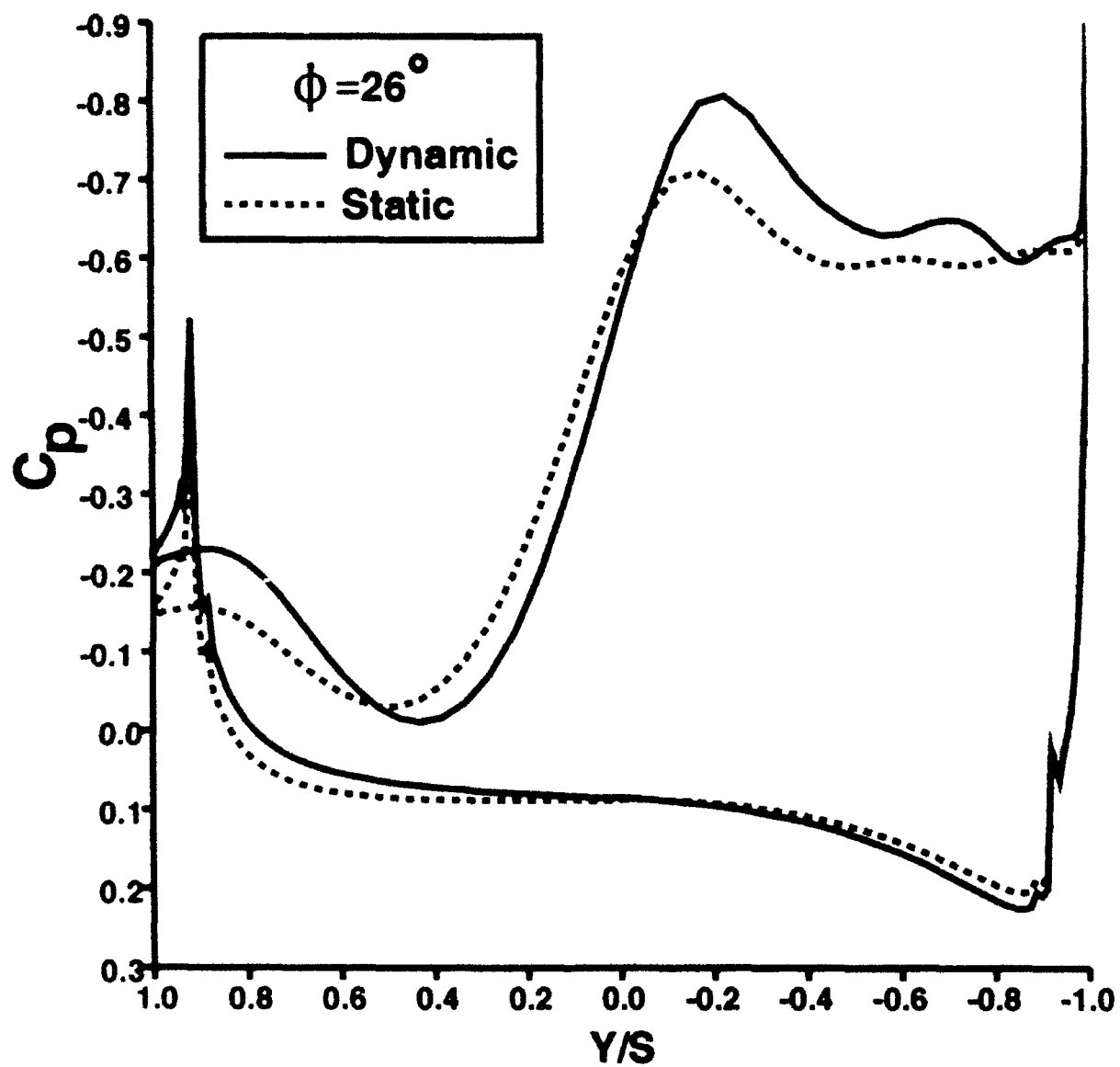
Figure 18. Comparison of Static and Dynamic Surface Pressure Coefficients: $X/L = 0.9$, $\phi = 26°$

is consistent with the differences in vortex location and vortex strength previously noted. Globally, the lift coefficient shows little difference between the dynamic and static condition. The static roll moment coefficient, however, shows a larger restoring moment than the dynamic case. This is primarily due to the lag in the position and strength of the left vortex during the roll maneuver.

6. Summary

Computations of a constant roll rate, $\Phi = 0.1325$, maneuver from $0°$ to $45°$ using a three-dimensional, Beam-Warming, Navier-Stokes solver have been presented. To demonstrate the capabilities of the numerical procedure, computational results for fixed roll angles of $0°$ and $45°$ and a Reynolds number of 400,000 are compared with the experimental measurements of Arena [8]. Good agreement with the measured surface pressure coefficients is obtained for both roll angles. The simulated surface oil flow showed excellent qualitative agreement with the experimental surface oil flow.

The computations of the roll maneuver were performed for a significantly lower Reynolds number, $Re = 10,000$, since no experimental measurements were available for this maneuver. This provides for added confidence in the computed results by eliminating questions of turbulence, transition, and the susceptibility to shear-layer instabilities. The reduction in Reynolds number primarily effects the secondary flow region and reduces the strength of the primary vortices.

The dynamical behavior of the vortices at a typical cross plane was described for the roll maneuver. The right vortex (downward leading edge) moves inboard and towards the surface while the left vortex (upward leading edge) moves outboard and away from the surface. A lag in the body-normal position of the left vortex similar to the lag observed for delta wing rock was noted. The left vortex continually loses strength during the roll maneuver. The right vortex initially gains strength but then rapidly loses strength as higher roll angles are achieved. A simple, quasi-static explanation of this vortex behavior based on the effective angle of attack and sideslip angles during roll is given.

The effect of the vortex behavior on the lift coefficient, roll moment coefficient, and surface pressure during the roll maneuver has also been described. The lift coefficient drops to 44% of its original value at $\phi = 45°$. The roll moment coefficient develops a minimum at $\phi = 31.55°$. The development of this minimum can be explained by the dynamic behavior of the vortices and their corresponding effect on the surface pressure coefficient.

7. References

[1] H. W. M. Hoeijmakers. Modeling and Numerical Simulation of Vortex Flow Aerodynamics. NLR-TP-91154-L, December 1990.

[2] L. E. Ericsson and J. P. Reding. Fluid Dynamics of Unsteady Separated Flow Part II. Lifting Surfaces. *Progress in Aerospace Sciences*, 24:249–356, 1987.

[3] T. Terry Ng, Gerald N. Malcolm, and Liane C. Lewis. Experimental Study of Vortex Flows over Delta Wings in Wing-Rock Motion. *Journal of Aircraft*, 29(4):598–603, July 1992.

[4] E. S. Hanff and S. B. Jenkins. Large-Amplitude High-Rate Roll Experiments on a Delta and Double Delta Wing. AIAA-90-0224, January 1990.

[5] Steven L. Morris and Donald T. Ward. A Video-Based Experimental Investigation of Wing Rock. AIAA-89-3349-CP, August 1989.

[6] D. Levin and J. Katz. Dynamic Load Measurements with Delta Wings Undergoing Self-induced Roll-Oscillations. *Journal of Aircraft*, 21(1), January 1984.

[7] L. T. Nguyen, L. Yip, and J. R. Chambers. Self-Induced Wing Rock of Slender Delta Wings. AIAA-81-1883, August 1981.

[8] Andrew S. Arena. An Experimental and Computational Investigation of Slender Wings Undergoing Wing Rock. Doctoral Dissertation of the University of Notre Dame, April 1992.

[9] Osama A. Kandil and H. Andrew Chuang. Computation of Steady and Unsteady Vortex-Dominated Flows with Shock Waves. *AIAA Journal*, 26(5):524–531, May 1988.

[10] Osama A. Kandil and H. Andrew Chuang. Unsteady Navier-Stokes Computations Past Oscillating Delta Wing at High Incidence. AIAA-89-0081, January 1989.

[11] J. T. Batina. Vortex-Dominated Conical-Flow Computations Using Unstructured Adaptively-Refined Meshes. AIAA-89-1816, June 1989.

[12] Osama A. Kandil and Ahmed A. Salman. Three-Dimensional Simulation of Slender Delta Wing Rock and Divergence. AIAA-92-0280, January 1992.

[13] Neal M. Chaderjian. Navier-Stokes Prediction of Large-Amplitude Delta-Wing Roll Oscillations Characterizing Wing Rock. AIAA-92-4428-CP, August 1992.

[14] Thomas H. Pulliam and Joseph L. Steger. Implicit Finite-Difference Simulation of Three-Dimensional Compressible Flows. *AIAA Journal*, 18(2):159-167, February 1980.

[15] Richard M. Beam and Richard F. Warming. An Implicit Factored Scheme for the Compressible Navier-Stokes Equations. *AIAA Journal*, 16(4):393-402, April 1978.

[16] Antony Jameson, Wolfgang Schmidt, and Eli Turkel. Numerical Solutions of the Euler Equations by Finite Volume Methods Using Runge-Kutta Time-Stepping Schemes. AIAA-81-1259, 1981.

[17] Thomas H. Pulliam and D. S. Chaussee. A Diagonal Form of an Implicit Approximate-Factorization Algorithm. *Journal of Computational Physics*, 39(2):347-363, February 1981.

[18] Man Mohan Rai and Sukumar R. Chakravarthy. An Implicit Form for the Osher Upwind Scheme. *AIAA Journal*, 24(5):735-743, May 1986.

[19] L. Bruce Simpson and David L. Whitfield. A Flux-Difference Split Algorithm for Unsteady Thin-Layer Navier-Stokes Solutions. AIAA-89-1995-CP, June 1989.

[20] Arthur C. Taylor III, Wing-fai Ng, and Robert W. Walters. Upwind Relaxation Methods for the Navier-Stokes Equations Using Inner Iterations. AIAA-89-1954-CP, June 1989.

[21] Raymond E. Gordnier and Miguel R. Visbal. Numerical Simulation of the Unsteady Vortex Structure over a Delta Wing. AIAA-91-1811, June 1991.

[22] Miguel R. Visbal. Numerical Investigation of Laminar Juncture Flows. AIAA-89-1873, June 1989.

[23] W. Phillip Webster and Joseph S. Shang. Thin-Layer Full Navier-Stokes Simulations Over a Supersonic Delta Wing. *AIAA Journal*, 29(9):1363-1369, September 1991.

[24] W. Phillip Webster and Joseph S. Shang. Numerical Simulation of Vortex Breakdown Over a Subsonic Delta Wing. AIAA-91-1814, June 1991.

[25] Miguel R. Visbal. Structure of Vortex Breakdown on a Pitching Delta Wing. AIAA-93-0434, January 1993.

[26] Micheal J. Stanek and Miguel R. Visbal. Investigation of Vortex Development on a Pitching Slender Body of Revolution. AIAA-91-3273, September 1991.

[27] Miguel R. Visbal. Structure of Laminar Juncture Flows. *AIAA Journal*, 29:1273 1282, August 1991.

[28] David L. Whitfield. Three-Dimensional Unsteady Euler Equation Solutions using a Flux Vector Splitting. Short Course on Numerical Grid Generation at Mississippi State University, June 1984.

[29] B. S. Baldwin and H. Lomax. Thin Layer Approximation and Algebraic Model for Separated Turbulent Flow. AIAA-78-0257, January 1978.

[30] David Degani and Lewis B. Schiff. Computation of Turbulent Supersonic Flows around Pointed Bodies Having Crossflow Separation. *Journal of Computational Physics*, 66(1):173–196, September 1986.

[31] Murray Tobak and David J. Peake. Topology of Three-Dimensional Separated Flows. *Annual Review of Fluid Mechanics*, 14:61–85, 1982.

[32] Dietrich Hummel. On the Vortex Formation over a Slender Wing at Large Angles of Incidence. In *High Angle of Attack Aerodynamics*, October 1978. AGARD-CP-247.

[33] Andrew S. Arena and Robert C. Nelson. An Experimental Study of the Nonlinear Dynamic Phenomenon Known as Wing Rock. AIAA-90-2812, August 1990.

[34] Nick G. Verhaagen and Steven H. J. Naarding. Experimental and Numerical Investigation of Vortex Flow over a Sideslipping Delta Wing. *Journal of Aircraft*, 26(11):971–978, November 1989.